Salivary gland stem cell-derived exosomes produced by a Wnt-loaded microwell culture accelerates the recovery from salivary gland dysfunction in murine salivary gland damage models

Jae-Min Cho

The Graduate School
Yonsei University
Department of Medicine

Salivary gland stem cell-derived exosomes produced by a Wnt-loaded microwell culture accelerates the recovery from salivary gland dysfunction in murine salivary gland damage models

A Dissertation Submitted
to the Department of Medicine
and the Graduate School of Yonsei University
in partial fulfillment of the
requirements for the degree of
Doctor of Philosophy in Medical Science

Jae-Min Cho

June 2024

This certifies that the Dissertation of Jae-Min Cho is approved.

Thesis Supervisor Jae-Yol Lim

Thesis Committee Member Chul Hoon Kim

Thesis Committee Member Won-Gun Koh

Thesis Committee Member Woong Sub Koom

Thesis Committee Member YoonHee Jin

The Graduate School
Yonsei University
June 2024

ACKNOWLEDGEMENTS

Above all, I would like to express my gratitude to Professor Jae-Yol Lim for this guidance throughout my Ph. D program. This thesis would not have been possible without his support and professional guidance. I am also sincerely grateful to Professor Won-Gun Koh, Yoonhee Jin, Woong Sub Koom and Chul Hoon Kim for their valuable advice. Their guidance enabled me to grow academically.

Many people have provided a great deal of assistance during my Ph. D Course. I would like to express my sincere gratitude to Dr. Yeo-Jun Yun who has consistently offered more help than anyone else and guided me in the right direction, as well as to my junior Ph. D candidates Seungyeon Hwang, Ye Jin Jung, and Yongpyo Hong.

I would like to express my gratitude to Dojin Choi my fellow researcher who has graduated and moved on, for being a source of inspiration during our time together in the research lab.

Furthermore, I would like to express my gratitude to Research Scientists Sujeong Ahn and Hyunsong Lee from the Chemical and Biological Engineering Laboratory for providing valuable research

materials. I am truly delighted to have had the opportunity to work alongside them.

Finally, I am obliged to give huge thanks to my parents. My mouther and father supported me and encouraged me to pursue me dream. My present state is impossible if there were no countless sacrifices from my parents. I hope I have made you proud as your son. I also give an equivalently large thanks to my brother for your endless support from the beginning of this journey. I wound like to express my appreciation to my family for providing me with their invaluable support.

TABLE OF CONTENTS

LIST OF FIGURES

ABSTRACT

Salivary gland stem cell-derived exosomes produced by a Wnt-loaded microwell culture accelerates the recovery from salivary gland dysfunction in murine salivary gland damage models

Background and objectives: The three-dimensional (3D) spheroid culture has been found to enhance stem cell properties such as differentiation potential and paracrine function. However, the potential benefits of harnessing the 3D spheroid culture for exosome production and regenerative application have not been fully investigated. This study aims to develop a microwell scaffold incorporating a biochemical niche to boost stemness and exosome production from salivary gland stem cells.

Methods: We fabricated a WNT3A protein (WNT)-loaded PLGA electrospun nanofiber that can enable sustained WNT release, mimicking the microenvironment of niche molecule release. This WNT-loaded nanofiber was integrated with a PCL microwell scaffold using an insert. Human salivary gland-derived epithelial stem cells (SG-EpSCs) were then cultured on either 2D plastic dishes or 3D bare PLGA nanofiber-PCL microwells (3DPLGA) and WNT-loaded PLGA nanofiber-PCL microwells (3DWNT). We then investigate the regenerative effects of SG-EpSC-derived exosomes produced in these microwells on salivary dysfunction using an irradiated murine salivary gland in mice and a human salivary organoid model.

Results: Fabricated PCL microwells and WNT3A-loaded PLGA nanofibers, which were subsequently micro-patterned onto PCL electrospun nanofibers. This resulted in a WNT3A-biosubstrate composite culture system featuring microwell arrays that secrete WNT3A into the wells. Our findings suggest that this novel WNT3A-secreting microwell culture system enhances stem cell characteristics, including increased marker expression, cell proliferation, and differentiation potential, as well as improved exosome production and secretion. Moreover, the

data indicate that canonical WNT signaling regulates the functional enhancement of SG-EpSC-derived exosomes in 3D spheroids cultured within WNT3A-secreting microwells. Recovery proceeded more rapidly in the 3D culture compared to 2D, with a significant increase in the number of proliferating cells observed in the 3DWNT condition. These results suggest that YWAHAZ, highly expressed in SG-EpSC-derived exosomes, significantly enhances the proliferation rate of salivary gland progenitor cells and increases phosphorylated PI3K-AKT expression, indicating its potential to improve salivary gland function.

Key words : Salivary glands; Epithelial; nanofibrous scaffolds; exosome; WNT3A; YWHAZ; Salivary organoids; Priming

1. INTRODUCTION

Salivary gland dysfunction can be caused by various factors, such as ductal obstruction, drugs, aging, autoimmune diseases, and radiation therapy for head and neck cancer. Radiation-induced damage can lead to irreversible stem cell depletion, which can affect oral homeostasis and lead to conditions such as dental caries and oral candidiasis. While multiple strategies have been employed to prevent salivary gland damage, there are limited clinical methods available to preserve function. Currently, cell-based therapies have emerged as a promising therapy. Extensive research has shown the therapeutic efficacy of mesenchymal stem cells (MSCs) in various diseases, and some of these therapies have already been approved by the Food and Drug Administration (FDA) in several countries. The therapeutic efficacy of MSCs is mainly attributed to their paracrine secretion of cytokines and growth factors, which have diverse cellular activities, such as immune modulation, anti-apoptotic effects, angiogenic effects, cytoprotection, and neurogenesis. Recent studies have shown that the paracrine effects of MSCs are not only due to these trophic factors but also to the secretion of exosomes.

Exosomes are small extracellular vesicles (EVs) ranging from 30 to 200 nm. They contain various molecules such as cytokines, growth factors, peptides, and nucleotides that allow cells to communicate with one another. Exosomes are often referred to as the "avatar" of their parent cells because they reflect the characteristics of the cells they originated from. For example, exosomes released by MSCs display properties similar to those of MSCs, including immune suppression, inflammation reduction, wound healing, and angiogenesis promotion. Administration of exosomes carries no risk of embolism, immune rejection, or tumorigenesis, unlike stem cell transplantation. Additionally, the probability of inducing an immune response is lower with exosomes than with stem cells. This makes allogeneic exosomes or even exosomes derived from plants suitable in addition to autologous exosomes. However, the therapeutic efficacy of exosomes may vary depending on the condition of the parent stem cells. Many researchers are working on ways to encourage stem cells to produce more exosomes or enhance stem cells to selectively amplify effective substances within exosomes.

Methods to improve stem cell stemness typically involve 3D cell culture and the use of niche factors. A 3D culture called spheroid culture has been found to promote stem cell properties by enhancing

cell-to-cell interactions. However, this method poses challenges due to the lack of an in vivo-like biochemical cue. Furthermore, traditional 3D culture often uses animal-derived extracellular matrix (ECM), so research has shifted towards using artificial matrices. In previous research, it was found that culturing MSCs from salivary glands in a 3D nanofiber scaffold improved their functionality and increased the expression of various growth factors. The stem cell niche is a complex cell signaling system, but synthetic biomaterials can be designed to mimic the natural ECM and modulate these interactions. In this study, we used a PLGA scaffold to continuously release WNT3A and culture salivary gland-derived epithelial stem cells (SG-EpSCs) under serum-free conditions. WNT proteins are crucial in stem cell proliferation, differentiation, and self-renewal. WNT-responsive stem cells are present in various tissues, including salivary glands. However, the WNT protein loses its activity in culture media, so a WNT-biomaterial composite culture system allowing the release of the WNT3A protein would be beneficial for priming stem cells in culture.

The WNT-loaded PLGA electrospun nanofiber scaffold facilitated the formation of 3D spheroids of SG-EpSCs. This resulted in significantly higher expression of stem cell-associated genes and proteins, as well as increased production of exosomes with enhanced paracrine activity. When these exosomes were infused into the salivary ducts of irradiated mice, they alleviated cell death following radiation exposure and promoted cell proliferation more effectively than exosomes from control media. The radioprotective effects were also demonstrated in an in vitro organoid culture. Exosomes from SG-EpSCs cultured on WNT3A-loaded microwell scaffolds contained high levels of YWHAZ, believed to activate the PI3K-AKT pathway and inhibit radiation-induced apoptosis in salivary gland acinar cells. These results suggest that 3D spheroid culture in WNT-releasing microwell scaffolds can enhance the production of exosomes and their function in the restoration of salivary gland hypofunction after radiation.

2. MATERIALS AND METHODS

2.1. PCL microwell

Polycaprolactone (PCL; MW 80,000), poly(ethylene glycol) diacrylate (PEGDA 575; MW 575), poly(D,L-lactide-*co*-glycolide) (PLGA) (Resomer® RG 503H; MW 24,000-38,000), 2-hydroxy-2-methylpropiophenone (HOMPP), 2,2,2-trifluoroethanol (TFE), phosphate-buffered saline (PBS; pH 7.4), Cell Counting Kit-8 (CCK8) were purchased from Sigma Aldrich (Milwaukee, WI, USA). Dulbecco's modified phosphate-buffered saline (DPBS), acetoxymethyl calcein (calcein-AM), and ethidium homodimer-1 (EthD-1) were purchased from Thermo Fisher Scientific (Waltham, MA, USA).

2.2. Manufacture of WNT3A-releasing microwells scaffolds

The WNT3A-loaded PLGA nanofiber-based microwell scaffolds (WNT3A + Microwell) were fabricated by combining electrospinning (NanoNC, Seoul, Korea) and photolithography processes. PCL microwells for cell spheroids formation were produced based on our previous study[99]. Briefly, PCL was dissolved in TFE in a 15 wt % ratio, and the solution was electrospun with the following conditions: a 0.5 mL/h flow rate, 8~10kV voltage, and 23G needle size. For photolithographic patterning, a hydrogel precursor solution was prepared by mixing PEGDA575 and deionized water in a 4:1 (v/v) ratio, and 2% (v/v) HOMPP as an initiator. To incorporate hydrogel micropatterns into the PCL nanofibers, 140 μL of a hydrogel precursor solution was dropped onto the 18×18mm^2 sized fibrous sheet which was then exposed to ultraviolet light (365 nm, EFOS Ultracure 100ss Plus, UV spot lamp) for 1s. WNT3A -loaded PLGA electrospun nanofiber was fabricated to enable sustained WNT3A release over seven days. PLGA 0.86 g was dissolved in 2mL of TFE, and 13.5μL of 0.2 μg/μL recombinant human WNT3A protein (WNT3A; R&D Systems, Cat # 5036-WN) in PBS was subsequently added to prepare WNT3A-loaded PLGA polymer solution. The prepared solution was electrospun by applying a voltage of 10kV to a 23G needle with 1 mL/h of flow rate for 1 hour and cut into 9×9mm^2 size. For comparison of WNT3A effect on the spheroids, bare PLGA nanofiber was also prepared with the same condition with WNT3A-loaded PLGA nanofiber only except for adding WNT3A in PLGA polymer solution. Fabricated PCL microwell and WNT3A-loaded PLGA

nanofiber were stacked and then fixed into Cellcrown™ 24 inserts (Scaffdex, Tampere, Finland) as shown in Figure 1B and C.

2.3. Characterization of WNT3A-releasing microwell scaffolds

The manufactured WNT3A + Microwell scaffolds were observed by scanning electron microscopy (SEM). The PCL microwell scaffold and PLGA nanofibrous sheets with and without loading WNT3A were dried overnight and then coated with platinum using a sputter coater (Cressington) at 15mA for 120s prior to SEM imaging. SEM images were obtained by field-emission scanning electron microscopy (JEOL-7001F) at a 10-kV accelerating voltage. For analysis of the PLGA nanofiber diameters, randomly chosen 100 fibers from the samples were measured by using SmartTiffV3 software from ZEISS. The depth profile of the microwell scaffold was measured using a surface profiler (Dektak XT stylus profiler, Bruker, Billerica, MA, USA).

2.4. WNT3A release test

The release of WNT3A was monitored *in vitro* for 7 days at specific time points using ELISA. The WNT3A-loaded PLGA nanofibers were immersed in PBS and stored at 37°C in an incubator (n = 6). The PBS was then collected at 1, 2, 3 hours and 1, 2, 3, 4, and 7 days after the initial immersion for analysis, while fresh PBS was added immediately after each collection. A sandwich ELISA was conducted with a WNT3A antibody and an HRP-conjugated WNT3A secondary antibody (Cusabio, Houston, TX, USA) following a conventional protocol. The final colorimetric change was measured with a spectrophotometric plate reader at 450 nm (VersaMax™ ELISA microplate reader, Molecular Devices, Sunnyvale, CA, USA).

2.5. Culture of human parotid gland epithelial stem cells into spheroids

Human Epithelial stem cells derived from human salivary gland (EpiSCs) were prepared from normal tissue samples of patients who underwent parotidectomy due to a benign parotid tumor after obtaining informed consent and institutional IRB approval (permission number #2015-10-001). In brief, tissue was cut into small pieces using a razor blade and digested with collagenase II #17101015, Thermo Fischer, Waltham, MA, USA) for 1 h. Cells were dissociated by TrypLE Express Enzyme #12604013, Thermo Fischer), filtered using 70 μm cell strainer, and then cultured with keratinocyte-

Serum Free Medium media (K-SFM, Gibco, ThermoFisher Scientific, Waltham, MA, USA) containing bovine pituitary extract (BPE, 50 μg/ml) and epidermal growth factor (EGF, 5 ng/ml). containing 10 uM Y27632 (#1254, Tocris, Abingdon, UK) ,1 uM A83-01 (#2939, Tocris) and 0.1 uM LDN193189 (#6053, Tocris) in humidified 5% CO_2 atmosphere at 37℃. Our previous observations optimized the optimal combination and concentration of small molecules. The sgEpSCs showed stem cell potential, such as high population-doubling time over the passage, differentiation capacity to SG epithelial cells, and sphere-forming ability, as described in the results. The EpiSCs with passages three to nine were used in this experiment. The cultures were divided into PCL microwells (PCL group), PCL microwells with bare PLGA nanofiber (PLGA group), and PCL microwells with WNT3A-loaded PLGA nanofiber (PLGA+WNT3A group). EpiSCs at passages 3 were expanded and seeded at a density of 7×10^4 cells per each microwell scaffold fixed in a 24-culture well. The seeded cells were cultured on scaffolds for 5 days to form uniform-sized spheroids. Although it takes 5 days for spheroids formation, we cultured 7 days to let the cell spheroids affected by WNT3A protein released from the PLGA nanofiber and to totally collect the exosomes secreted from the spheroids.

2.6. Cell morphology, viability, and proliferation

A CCK8 assay was conducted to assess the proliferative ability of the EpiSCs on the scaffolds. Briefly, EpiSCs were cultured on scaffolds in a 24-well plate at a density of 7×10^4 cells/scaffold, and cell proliferation was analyzed at 1, 3, and 5 days after culture. After adding 10% (v/v) of CCK8 solution in cell culture media and incubating at 37°C for 3 hours, EpiSCs proliferation was determined by measuring the absorbance at 450 nm using a 96-well plate reader (Molecular Devices, San Jose, CA, USA). At least three independent cell viability and proliferation analyses were performed.

2.7. Exosome Extraction and Purification

After 72 h of culture, the EpiSCs (Epithelial Derived Stem Cells) culture medium was harvested and centrifuged at 300g for 10 min and 2000g for 10 min to remove residual cell debris. The remaining supernatant was passed through 0.22-μm PES membrane filter (CellTreat) and then concentrated using 10 kDa Amicon ultra-15 centrifugal filters (Millipore). Total exosome isolation reagent (from cell culture media, Invitrogen) was then added in a 1:1 ratio to the volume obtained

after the Amicon-based concentration process. The solution was mixed by vortexing for 1 min and incubated overnight at 4°C. The next day, the precipitated exosomes are recovered by standard centrifugation at 10,000 x g for 60 min at 4°C. The concentrated solution was centrifuged at 10,000 × g for 60 min at 4°C, and the pellet was resuspended in steriled PBS. The pelleted exosomes were resuspended in 100 μL of phosphate-buffered saline solution (PBS) and quantified by micro BCA protein assay kit (R23235, Thermo Fisher, USA). Exosomes were then assessed by transmission electron microscopy (TEM) and nanoparticle tracking analysis (NTA), as per previously described protocols. Exosomes were further verified by western blot analysis of exosome-associated markers including CD9, CD81, HSP70, Calnexin, and TSG101.

2.8. Nanoparticle Tracking Analysis (NTA)

To determine the size distribution and particle concentration, Stem cell-derived exosomes diluted with PBS were analyzed by nanoparticle tracking analysis (NTA) using a NanoSight NS300 (Malvern Panalytical, Amesbury, UK) equipped with a 642-nm laser. Stem cell-derived exosomes, diluted with PBS to between 20 and 80 particles per frame, were scattered and illuminated by the laser beam and their movements under Brownian motion were number of captures 3 times and captured for 60 s each at a camera level of 15. Videos were then analyzed by the NTA 3.2 software using constant settings. To provide a representative result, at least 5 videos were captured and >2000 validated tracks were analyzed for each sample. The NTA instrument was regularly checked with 100 nm-sized standard beads (Thermo Fisher Scientific). To provide representative size distribution of exosomes, size distribution profiles from each video replicate were averaged.

2.9. Transmission Electron Microscopy (TEM)

A 20 μl solution of exosomes was placed on a copper mesh and post-negatively stained with 2.5% glutaraldehyde in 0.1 M sodium cacodylate solution (Ph 7.4) for 10 min. The sample was then dried for 5 min under incandescent light. Fixed suspensions containing exosomes were spotted on Formvar® coated copper grids (CF200-Cu, Electron Microscopy Sciences, USA) for 30 s. Samples were negatively stained with 2% uranyl acetate in water for 3 min and dried with filter paper. was observed and photographed under a transmission electron microscope (JEM-2100plus, JEOL Inc., Japan). The diameter of the particles was analyzed using JEM-2100 plus software.

2.10. Western Blot

Cell, organoid pellets, and tissue were collected and resuspended in RIPA lysis and extraction buffer (Invitrogen, ThermoFisher Scientific, Waltham, MA, USA). The resuspended cell pellet was vortexed for 30 s and then incubated on ice for 20 min and centrifuged at 20,000 × g for 30 min. The supernatants were collected for Western blot analysis. (10% SDS-polyacrylamide gel electrophoresis; 20 μg protein/lane). The resolved proteins were transferred to a PVDF (polyvinylidene difluoride) membranes (Cat. #1620167, Bio-Rad) using Trans-Blot Turbo Transfer System (Bio-Rad). Membranes were blocked in 5% skim milk for 1 h at room temperature and incubated with primary antibody overnight at 4 °C with slow shaking. Using rabbit polyclonal antibody CD9 (Cell Signaling Technology, Danvers, MA, USA), CD81 (Cell Signaling Technology), TSG101 (Cell Signaling Technology) and calnexin (Cell Signaling Technology). The proteins were visualized using an enhanced chemiluminescence system (Thermo Fisher Scientific, MA).

2.11. Sample Preparation for Proteomic Analysis

The exosome samples were washed with phosphate-buffered saline (PBS) solution and stored at −80 °C until use[25]. Tissue (100 mg) was homogenized in modified RIPA buffer (50 mM Tris–HCl, 150 mM NaCl, 1% NP-40, and 0.25% sodium deoxycholate, pH 7.4) containing a protease inhibitor (Sigma-Aldrich, St. Louis, MO), and the supernatant was collected via centrifugation at 15, 000 rpm for 30 min. The protein concentration was determined using a micro BCA protein assay kit (ThermoFisher Scientific, Waltham, MA, USA). After lysis, we concentrated and purified the cell lysates using Amicon Ultra centrifugal filters (Millipore, Billerica, MA). The experiment was initiated with 100 μg of protein to minimize loss during the desalting process. The protein was diluted in 50 μL, and 1 μL of the solution was then injected into the liquid chromatography with tandem mass spectrometry (LC/MSMS). Therefore, the total amount of each peptide was 1 μg. The peptide samples from the in-solution digestion were desalted with an Oasis HLB column (Waters, Milford, MA) and lyophilized using a speed vac. Next, the peptides were dissolved in 0.1% formic acid and 3% acetonitrile (ACN) in a volume of 50 μL, and 1 μL was loaded onto a nano-LC-MS/MS.

2.12. Tissue isolation and culture of mouse salivary gland organoids

Only SMG was obtained from three types of murine major salivary glands (PG, SMG, and SLG) in female C57BL/6 mice aged 6 weeks of age. Mice were purchased from the Jackson Laboratory (Bar Harbor, ME, USA), fed ad libitum, and maintained at 22 ± 2 °C, 50 ± 10% relative humidity for 12 h of the light-dark cycle (8 a.m.–8 p.m.) under specific pathogen-free conditions in a facility accredited by AAALAC International (#001071). All experiments were approved by the Institutional Animal Care and Use Committee (approval number #2018-0071) at Yonsei University College of Medicine. Both murine salivary gland tissues were cut into small fragments using a razor blade. Fragments were enzymatically digested initially with collagenase type II (#17101015, Thermo Fischer, Waltham, MA, USA) for 1–2 h depending on the tissue size, and subsequently with TrypLE Express (#12604013, Thermo Fischer) for 10 min. Cells were passed through a 70 μm strainer, embedded in growth factor-reduced Matrigel (#356231, Corning, Corning, NY, USA), and supplied with a medium containing relevant growth factors and small molecules. Mouse GEM contained Advanced DMEM/F12 (#12634010, Thermo Fischer) DMEM/F12 (Thermo Fisher Scientific, Waltham, MA, United States) with penicillin/streptomycin (Gibco, Grand Island, NY, United States), HEPES (Biowest), and GlutaMAX (Gibco). Supplemented with 5 nM NRG1 (#100-03, Peprotech, Cranbury, NJ, USA), 1% homemade RSPO1 CM or 100 ng/mL recombinant RSPO1 (#120-38, Peprotech), 100 ng/mL Noggin (#120-10 C, Peprotech), 5 nM FGF1 (#450-33 A, Peprotech), 1 nM FGF7 (#450-60, Peprotech), 10 μM Y-27632 (#1254, Tocris, Abindon, UK), and 0.5 μM TGFβ inhibitor A83-01 (#2939, Tocris). For the differentiation of murine salivary gland organoids, Y-27632 was removed 7 days after seeding. The medium (500 μL/well) was added and changed every 2–3 days. The organoids were maintained at 37°C in a humidified atmosphere under 5% CO2[104].

2.13. Exosome uptake assay

Exosomes were pre-stained with PKH26 using a PKH26 Red Fluorescent Cell Linker Kit For general cell membrane labeling (Sigma-Aldrich, St. Louis, MO, USA). Human parotid gland epithelial stem cells (EpiSCs $2 \times 10^{\wedge 6}$/well) were seeded in 6-well plates and 2 μg of PKH26-labeled exosomes were added to the culture. After incubation for 24 h, cells were fixed with 4% paraformaldehyde and DAPI was used to stain the nuclei. The location of exosomes was observed under an Axio Imager M2 (Carl Zeiss, Jena Germany).

2.14. Internalization of PKH26-labelled exosomes in EpiSCs

Purified EVs derived from sgEpSCs were labeled with a PKH26 red fluorescence labeling kit (Sigma-Aldrich, MO, USA). EVs were incubated with 2 μM of PKH26 for 5 min and washed five times using a 100 kDa filter (Microcon YM-100, Millipore) to remove excess dye. PKH26-labelled EVs were used to assess EV uptake in vitro and in vivo.

2.15. In vivo animal experiments

Adult female C57BL/6 mice, 8 weeks of age, were purchased (Orient Bio, Gyeonggi-Do, Korea) and fed with food and water ad libitum. All the procedures were approved by Institutional Animal Care and Use Committee (IACUC) in Yonsei University College of Medicine and conformed to Avison Biomedical Research Center (ABMRC) guidelines. The experimental groups consisted of five groups; non-irradiated and PBS-administered group (Control, healthy control), irradiated and PBS administered (PBS), irradiated and 2-dimensional culture exosomes-administered group (2D), Exosome-administration group using PLGA scaffold ($3D^{PLGA}$), and exosome-administration group using WNT3A scaffold. ($3D^{WNT3A}$). The particle count was measured with NTA and the samples were diluted accordingly. The fractionated irradiation was conducted for 1 h before exosomes or control administration. Irradiation was performed on the salivary glands in three fractions into 7.5 Gy doses with alpha rays (dose rate: 7.5 Gy/3 min) using an experimental irradiator (X-rad320, Alphatech International, Auckland, and Sydney). After irradiation, either 2D, $3D^{PLGA}$ and $3D^{WNT3A}$ at a concentration of $1x10^{\wedge 9}$ of particles / 20 μL was injected at a rate of 20 μL/min for 3 consecutive days. Retroductal delivery was performed via a cannula inserted into the submandibular duct orifice as described in our previous paper[26].

2.16. Salivary gland weight and function evaluation

After 12 weeks of exosome administration, mice were euthanized, the extirpated SMGs were weighed, and compared among groups. Body weights were measured during the follow-up period. Before extirpation, mice were anesthetized using Ketamine® (100 mg/kg, Yuhan Corporation, Seoul, Korea) and Rompun® (10 mg/kg, Bayer HealthCare, Mississauga, Ontario, Canada). Mice were then intraperitoneally administered with muscarinic agonist pilocarpine (5 mg/kg) to stimulate saliva secretion. Saliva was collected from the floor of the mouth using a micropipette 5 min after

stimulation. The collected saliva was placed in pre-weighed 1.5-mL microcentrifuge tubes, and salivary flow rate (SFR) (μL/min) was calculated by dividing the total volume (μL) of the total collected saliva by the collection time (min) and weight of SMGs (mg) was defined as the time from stimulation to the beginning of saliva secretion.

2.17. Tissue histology

Whole-mount salivary gland organoids and mouse tissue section histological analysis have been previously described[27]. In brief, tissue was fixed with 10% Neutral Buffer Formalin (10% NBF) for 24h. Then the tissue was dehydrated and embedded with paraffin. Paraffin sections (2 um thick) were dewaxed using xylene for 30 min. Sections were stained with hematoxylin and eosin (H&E, Abcam, Cambridge, UK) for histological examination and Masson's trichrome (MTC, Abcam), and periodic acid–Schiff (PAS, Abcam) staining according to the manufacturer's instructions. Two blinded examiners assessed the pathological changes, identification of mucosubstances (PAS), inflammation and structure damage (H&E), and total fibrosis (MTC). Staining scores were recorded as 0–5 based on the following criteria: staining intensity was scored as 1 for 5% or less, 2 for 5% to 20%, 3 for 20% to 50%, 4 for 50% to 80%, and 5 for 80% or more stained cells. Fibrosis level and mucus area were measured as blue for MTC and magenta color for PAS as area ratios. Two blind examiners scored SMG structural damage and measured the ratio of mucin-containing area.

2.18. TUNEL assay

Apoptotic cells in SMG tissues were analyzed using terminal deoxynucleotidyl transferase-mediated dUTP nick-end labeling (TUNEL) staining using an apoptotic cell detection kit (Millipore, Billerica, MA, USA) at 37 °C for 60 min in the dark according to the manufacturer's instructions. Cells were counterstained for 5 min using DAPI (Vector Labs, San Diego, CA, USA). TUNEL-positive cells had pyknotic nuclear fragments that were stained dark green after the fluorescent staining of apoptotic cells. Apoptotic cells were quantified by assessing the number of TUNEL-positive cells from three randomly selected fields per slide from each mouse using a blinded examiner. All fluorescence images of the sections were obtained using an Axio Imager M2 microscope (Carl Zeiss).

2.19. Histochemistry and immunohistochemistry

Tissue samples were fixed with formalin and embedded in paraffin. Following dewaxing and rehydration, immunofluorescence-stained using a heat-induced epitope retrieval was performed by boiling the specimens in Tris-EDTA buffer (pH 9.0) at 98 °C for 45 min. With 5% normal goat serum as the blocking solution. Subsequently, the slides were washed in Tris-Buffered Saline (TBS) before followed by incubation with primary antibodies overnight at 4 °C. The following primary antibodies were used for IHC or IF experiments; KRT5 (#905904, 1:1000; Biolegend, San Diego, CA, USA), KRT7 (#ab181598, 1:500; Abcam), KRT14 (#ab7800, 1:500; Abcam), MIST1 (#ab187978, 1:250; Abcam), AQP5 (#sc-514022, 1:1000; Santa Cruz, Dallas, CA, USA), MUC10 (#orb101843, 1:250; Biorbyt, Cambridge, UK), Cleaved Caspase-3 (#9661, 1:500; Cell Signaling, Danvers, MA, USA), gH2AX (#80312, 1:500; Cell Signaling, Danvers, MA, USA), PCNA (#2586, 1:1000; Cell Signaling, Danvers, MA, USA), p-PI3K (#4228, 1:200; Cell Signaling, Danvers, MA, USA), and p-AKT (#4060, 1:200; Cell Signaling, Danvers, MA, USA). Biotinylated secondary antibodies and Pierce DAB substrate kit (#34002, Thermo Fischer) were used for IHC. For IF, the following secondary antibodies were used at 1:500 dilution; Donkey anti-Mouse IgG, Alexa Fluor™ Plus 488 (#A32766, Invitrogen), Donkey anti-Rabbit IgG, Alexa Fluor™ Plus 488 (#A32790, Invitrogen), Donkey anti-Mouse IgG, Alexa Fluor™ Plus 555 (#A32773, Invitrogen), Donkey anti-Rabbit IgG, Alexa Fluor™ Plus 555 (#A32794, Invitrogen), Donkey anti-Goat IgG, Alexa Fluor™ Plus 555 (#A32816, Invitrogen), Donkey anti-Rabbit IgG, Alexa Fluor™ Plus 647 (#A32795, Invitrogen), Alexa Fluor 488 AffiniPure Donkey Anti-Chicken IgY (#703545155, Jackson ImmunoResearch, West Grove, PA, USA), and nuclei were counterstained with Hoechst 33342 (#R37605, Thermo Fischer). The data were analyzed with NIS-elements BR (Nikon) or ZEN (Carl Zeiss) software.

2.20. Quantitative real-time polymerase chain reaction analysis

Total RNA was isolated from the cultured organoids and mouse tissue using TRIzol Reagent (Invitrogen, Carlsbad, CA, USA), and 1 μg of total RNA was subjected to first-strand cDNA synthesis (Takara Bio, Shiga Ontario, Japan), according to the manufacturer's instructions. Gene expression was assessed by the conventional SYBR method using the QuantStudio 5 Real-Time PCR Systems (Applied Biosystems). Primer information for analysis of mouse and human genes. Gene expressions were normalized to the expression of GAPDH. The amplification program

consisted of 35 cycles of denaturation at 95 °C for 5 s, annealing at 55 °C for 20 s, and extension at 72 °C for 20 s. Sample quantification was performed according to the threshold cycle using the ΔΔCt method. The values presented in the graphs are mean ± SD values.

2.21. Statistical analysis

Statistical analysis was performed using Prism software (GraphPad® Software, Inc., CA, USA), and statistical significance was defined as $^{*}P < 0.05$, $^{**}P < 0.01$, and $^{***}P < 0.001$ for comparison to 2D group; $^{\#}P < 0.05$, $^{\#\#}P < 0.01$ and $^{\#\#\#}P < 0.001$ for comparison to $3D^{PLGA}$ group; $^{\$}P < 0.05$, $^{\$\$}P < 0.01$, and $^{\$\$\$}P < 0.001$ for comparison to the $3D^{WNT}$ group. One-way ANOVA using Tukey's post-hoc test was used to compare groups; Control: (healthy control); PBS: PBS injected after irradiation (Positive control or Disease group); 2D: treated with 2D culture exosomes; $3D^{PLGA}$: treated with PLGA scaffold culture exosomes; $3D^{WNT}$: treated with WNT3A scaffold culture exosomes.

3. Results

3.1. Characterization of WNT3A-releasing microwell scaffolds

Figs. 1 A and B depict a manufacturing process of the WNT3A-releasing microwell scaffolds. Fig. 1C shows the completed images of the scaffold for culture in a 24-well plate. This WNT3A-releasing microwell scaffold enabled spheroids formation, sustained release of WNT3A, and their influence on the cells during the culture to improve function-enhanced exosome secretion from the cells, as shown in Fig. 1D. The combination of electrospinning and photopatterning techniques produced a well-defined microwell array consisting of a PEG hydrogel wall and PCL nanofibers as shown in the SEM images (Fig. 1E). Surface profile data revealed that the depth of the microwell was approximately 128 μm (Fig. 1F). The morphology and thicknesses of the PLGA nanofibers with and without loading WNT3A were analyzed through SEM examination (Fig. 1G and 1H). The similar average diameters of the bare PLGA and WNT3A-loaded PLGA nanofibers, which resulted in 3.2076 ± 0.6043 μm and 3.2095 ± 0.8896 μm, respectively, demonstrate that the two nanofibers have no significant difference and thus suitable to compare for control experiment. Although the magnified SEM images of the nanofibers in Fig. 1G showed a different morphological feature such as the rough surface of WNT3A-loaded PLGA nanofiber strands, this resulted from the existence of WNT3A protein since the protein's structural heterogeneity and surface charge affects the electrospinning process.

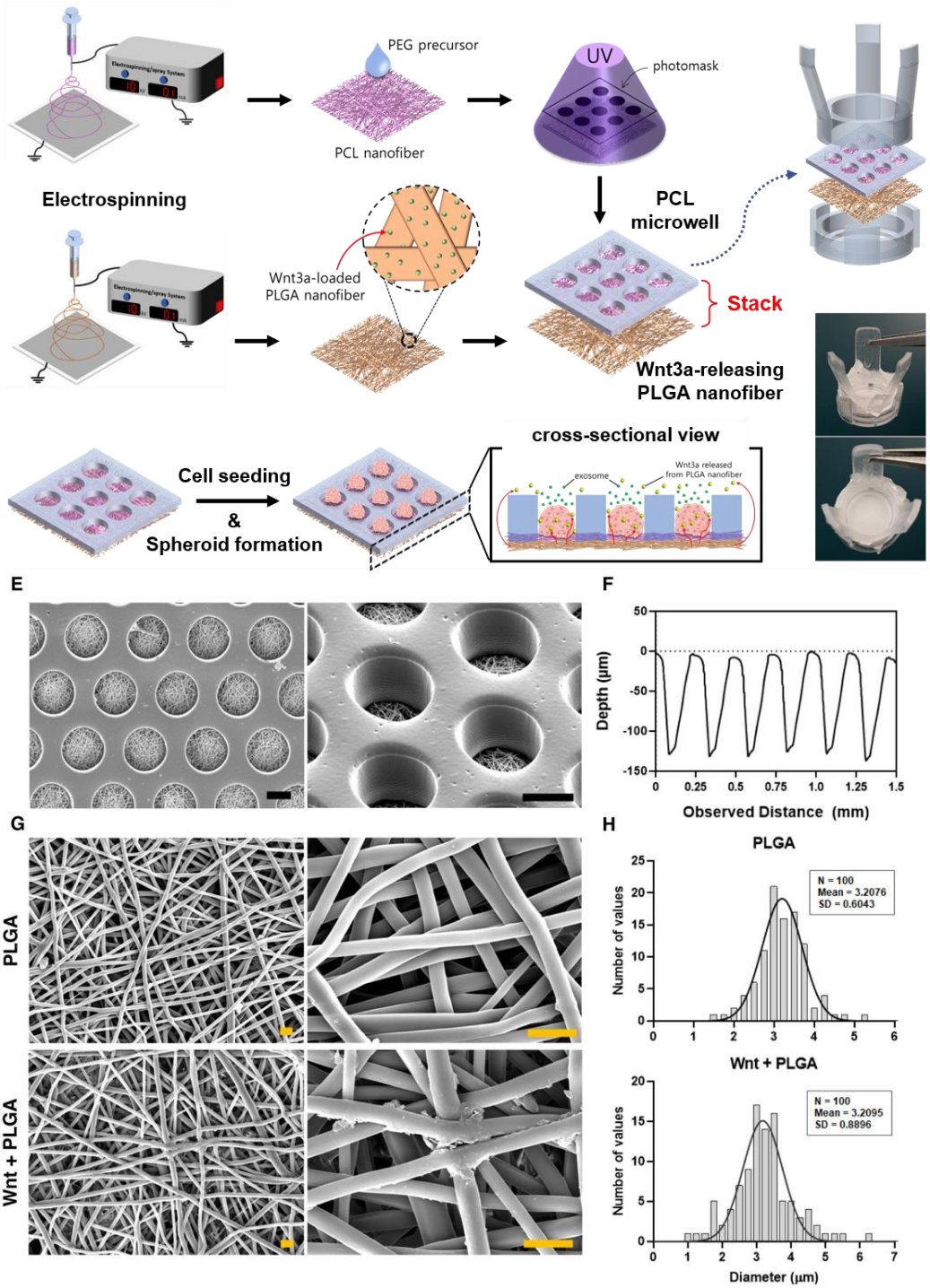

Figure 1. Schematic representation of the overall procedure for manufacturing insert-integrated WNT3A-releasing scaffolds. (A) Fabrication process of PCL microwells and WNT3a-releasing PLGA nanofiber. (B) Stacking method of PCL microwells and WNT3A-loaded PLGA nanofiber using insert. (C) Images of fabricated insert-integrated WNT3A-releasing scaffold. (D) Schematic representation of cell seeding and spheroid formation on WNT3A-releasing scaffold. (E) SEM images of PCL microwells (scale bar = 100μm). (F) Surface profiler of PCL microwells. (G) SEM images and (H) diameter distribution of bare PLGA nanofibers and WNT3A-loaded PLGA nanofibers. (scale bar = 10μm).

3.2. Release profile of WNT3A and cell viability

SG-EpSCs were seeded onto the Microwell, PLGA+Microwell, and WNT3A+Microwell groups and cultured for 5 days. To identify the cell morphology and viability, a Live/Dead assay was conducted for days 1, 3, and 5 (Fig 2A). This result indicates that once the cells were attached to the PCL nanofiber layer after their seeding process, they grew and aggregated well during the culture, which leads to successful spheroids formation. Spheroids formations were observed in the PCL microwell layer of all groups within 5 days. The existence of the PLGA nanofiber layer had any negative influence on the cell culture, which was determined by comparison of the PCL group, PLGA group and PLGA+WNT3A groups. The SG-EpSCs were more densely assembled as spheroids in the PLGA+WNT3A group than in the PCL and PLGA groups. To detect the proliferation of SG-EpSCs cultured on PCL, PLGA group, and PLGA+WNT3A group, a CCK8 assay was performed within 5 days. As shown in Fig. 2B, the cells seeded on all three groups proliferated well within 5 days of culture, indicating that PCL, PLGA group, and PLGA+WNT3A group cultures induced no significant cytotoxicity. PCL and PLGA groups had no significant differences in the measured value of the number of cells proliferated for each day 1, 3, and 5, which represents that the PLGA nanofiber layer including its by-products produced by the hydrolysis of PLGA in the culture medium did not affect during the cell culture and spheroids formation at all. According to this result, we decided to exclude using the PCL group and rather use only the PLGA group as a 3D spheroid cell culture group without WNT3A protein, as a control group of WNT3A+PCL, for further in vitro and in vivo assessment. Among the three groups, the WNT3A+PCL group showed the best proliferative ability compared to the other two groups. The release of the WNT3A from PLGA nanofibers of our WNT3A-releasing scaffold was determined by ELISA assay upon recombinant human-WNT3A. Fig. 2C shows a cumulative release profile of WNT3A proteins within 7 days. The initial burst was observed within 4 hours after immersing in PBS at 37°C condition and then showed a linear release profile until day 4. From day 4 to day 7, the release rate decreased compared to the previous days. 33ng of the WNT3A protein was initially loaded on one scaffold, and the total amount of the WNT3A protein released from the scaffold within 7 days was measured to 20.26439 ± 0.219376 ng. As a result, we verified that our scaffold has about 61.4% yield of the WNT3A protein release. There results demonstrated that our scaffold was successfully designed to enable sustained release of the protein completely within 7 days to affect the cell function during the culture since the cell spheroids formation on our scaffold takes 5 days

and we harvest the exosome on the seventh day of the culture.

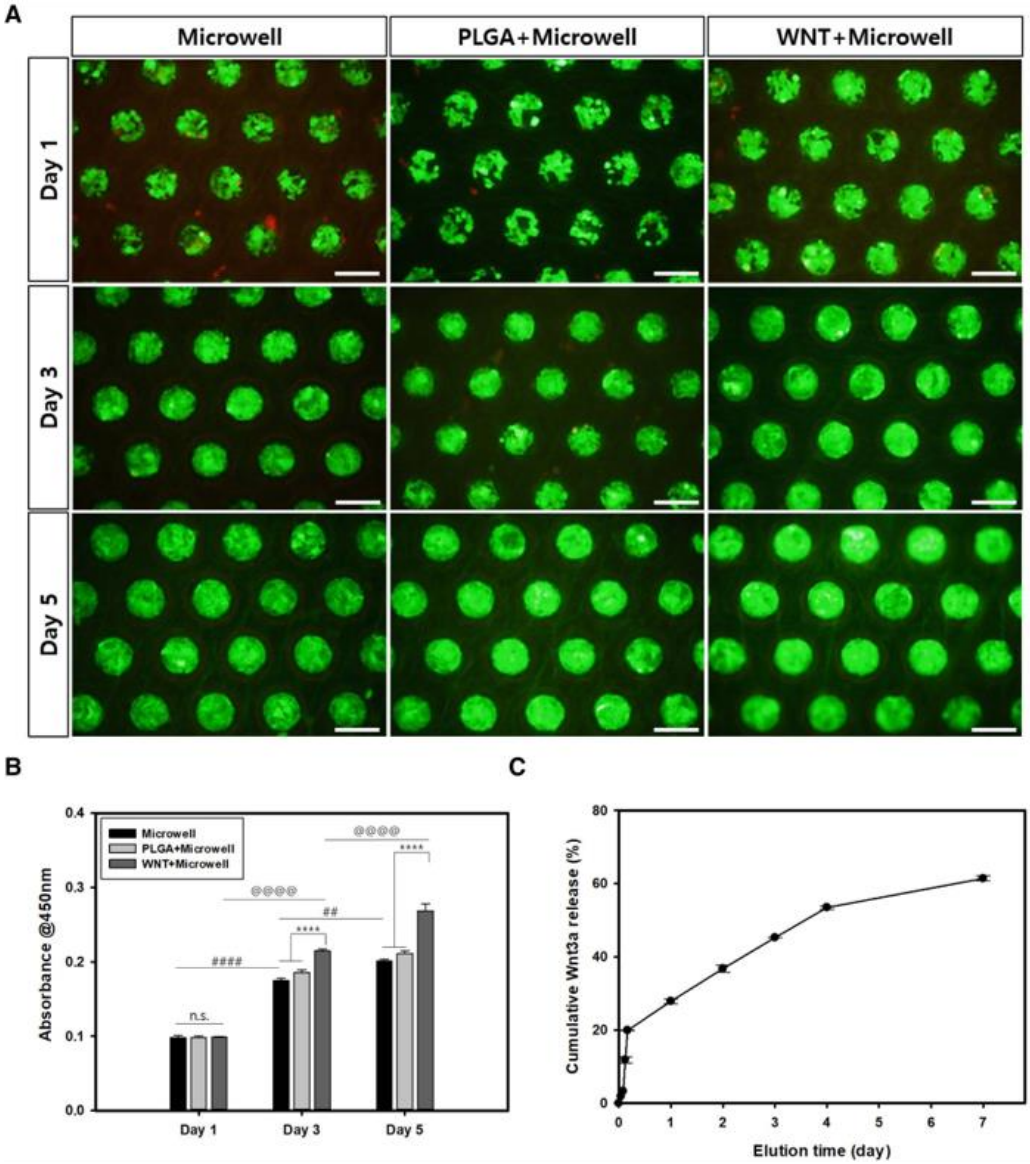

Figure 2. WNT3A release profiling and cell viability assessment of SG-EpSCs in PLGA-microwells. (A) Live/Dead fluorescence images of SG-EpSCs cultured on the scaffolds (scale bar = 200μm). (B) Cell viability results of SG-EpSCs cultured on Microwell, PLGA + Microwell, and WNT3A/PLGA + Microwell scaffolds for day 1, 3, and 5. (C) Cumulative WNT3A release profile

of WNT3A -releasing scaffold. ELISA assay upon recombinant human-WNT3A was conducted twice with n=3 for each trial.

3.3. Characterization of SG-EpSCs derived exosomes

While all cells are known to release exosomes, it is reported that rapidly dividing cells release a greater amount of exosomes. Therefore, we aimed to measure the released exosomes from cells cultured in 2D (hereafter, 2D), cells cultured in PLGA microwells for 3D culture (hereafter, $3D^{PLGA}$), and cells cultured in WNT3A+PLGA microwells where WNT3A (hereafter, $3D^{WNT}$) is released to validate this hypothesis. To test our hypothesis, first, we isolated exosomes from the supernatant of equal amount of endpoint cell numbers of each cell culture conditions by sequential centrifugation (Fig. 3A). Nanoparticle tracking analysis (NTA) revealed that the average diameter of the most common particle is 120.9 nm, and the distribution histogram further showed that the diameter of this particle was concentrated in the range of 120–150 nm (Fig. 3B-D). Exosome particles derived from $3D^{PLGA}$ and $3D^{WNT}$ increased compared to those derived from 2D. This interpretation is supported by the large range in scattering intensity observed across EV size in the nanoparticle tracking analysis data (Inserted panel of Fig. 3B-D). EV concentration per 1 mL increased from 2D to $3D^{PLGA}$ and further increased from $3D^{PLGA}$ to $3D^{WNT}$. The amount of EVs released per cell also showed consistent results across these conditions (Fig. 3E-F). On the other hand, the average diameter of EVs was larger than that of $3D^{PLGA}$ in 2D, and $3D^{PLGA}$ was found to be larger than $3D^{WNT}$ (Fig. 3G). The measurements of EVs released in each culture condition using transmission electron microscopy also confirmed consistency in EV size with the results obtained from NTA (Fig. 3H-J). Furthermore, the culture environment not only altered the release of EVs from cells but also, upon comparing EVs of the same quantity through western blot, revealed higher expression of the representative tetraspanin family markers CD9 and CD81 in $3D^{PLGA}$ and $3D^{WNT}$ compared to 2D (Fig. 3K). Conversely, calnexin, used as a cell surface marker, showed higher expression in 2D. Collectively, in summary, 3D culturing using WNT3A protein-secreting scaffolds increased the growth of SG-EpSCs cells, thereby enhancing the quantity of EVs released per cell.

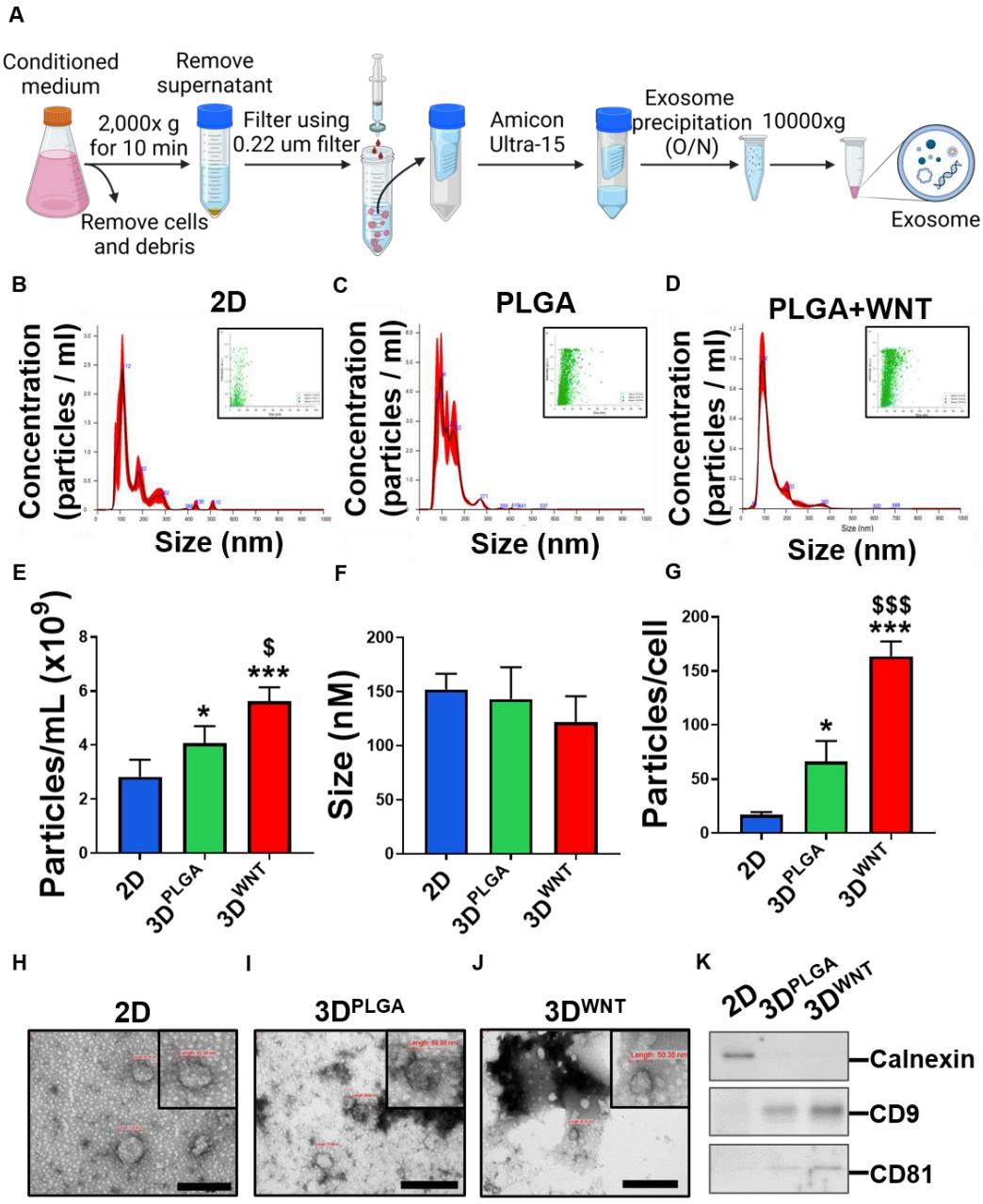

Figure 3. Validation and characterization of exosome fractions isolated from various culture conditions. (A) Protocol of the exosome isolation and purification from FBS-free media (K-SFM).

(B-D) Measurement of the microvesicle concentration by nanoparticle tracking analysis (NTA). (upper panel) Scattering distributions are presented from three consecutive 60 s runs for each sample (n = 5). (E) Quantification of the number of secreted EVs. (F) Particle number per cell for 2D, $3DP^{LGA}$ and $3D^{WNT}$ (n=5). (G) Quantification of the size of secreted EVs. (H-J) Representative TEM images of exosomes isolated from SG-EpSCs confirm the expected cup-shaped morphology of vesicles seen in three different exosomes. (K) Detection of exosomal positive markers CD9, CD81, and exosomal negative marker Calnexin by western blotting (20 μg protein per each lane). Data are presented as the mean cell number ± SEM. One-way ANOVA and Tukey's post-hoc test were used to compare groups. *compared to 2D; $^{\$}$compared to $3D^{PLGA}$. *P < 0.05, ***P < 0.001, $^{\$}$P < 0.05, $^{\$\$\$}$P < 0.001.

3.4. Retroductal exosome administration reduces radiation-related morbidity and evaluates the functional changes in gland function.

When the mouse salivary glands are irradiated, nearly all acinar and ductal cells suffer irreversible loss. To investigate the role of EVs in the salivary gland dysfunction model, salivary gland dysfunction was induced by irradiation three times, and 2D, $3D^{PLGA}$, and $3D^{WNT}$ exosomes were administered three times for three days. Salivary glands were analyzed at 2 and 12 weeks post-irradiation. (Fig. 4A). Final body weights at 12 weeks post-irradiation significantly differed among the groups (Fig. 4B). We found that IR-induced body weight loss in 35-40% of irradiated mice (PBS) at 12 weeks post-IR possibly due to loss of saliva and decreased oral intake. And, the average body weights were greater in the 2D, $3D^{PLGA,}$ and $3D^{WNT}$ groups than in the PBS group. As a result of measuring the gland size and gland weight, it was found to be smaller in the 2D group than in the $3D^{PLGA}$ and $3D^{WNT}$ groups, and the gland size in the PBS group was the smallest (Fig. 4C, D). At 12 weeks post-IR, the PBS group showed a significantly reduced ability to produce saliva with decreased SFR and prolonged salivation lag time, compared with the control group (Fig. 4E, F). Both SFR and lag time were significantly improved in the 2D, $3D^{PLGA}$, and $3D^{WNT}$ groups, compared with the PBS group, at 12 weeks post-IR. Both SFR and lag time were significantly improved in the 2D, $3D^{PLGA}$, and $3D^{WNT}$ groups, compared with the PBS group, at 12 weeks post-IR. The $3D^{WNT}$ group showed more effective SFR and lag time improvement at 2- and 12-weeks post-IR than the 2D, $3D^{PLGA}$ group (Fig. 4E, F). In addition, a chronic salivary gland damage model induced by radiation, utilizing mice that had passed 12 weeks post-exposure, was examined using special staining techniques such as hematoxylin and eosin (H&E), periodic acid–Schiff (PAS) and Masson's trichrome (MTC) staining. Histologically, IR-induced salivary gland showed epithelial desquamation, vacuolation, loss of acinar and duct structure, and inflammatory cell infiltration. Exosome treatment decreased the IR-induced increase in epithelial desquamation, vacuolation, loss of acinar and duct structure, and inflammatory cell infiltration compared with IR-treated salivary gland (Fig. 4G). Moreover, the average total damage score was lower in the $3D^{PLGA}$ group than in the 2D group, and lower in the $3D^{WNT}$ group than in the $3D^{PLGA}$ group (Fig. 4J). Mucin-producing acini were assessed by quantification of magenta-colored areas (Fig. 4H). Degrees of fibrosis were evaluated by measuring blue areas after MTC staining (Fig. 4I). The results of morphometric analysis revealed that fibrosis increased and mucin-containing area decreased significantly after irradiation. However, compared to the PBS-administered group, fibrosis decreased and mucus

production area increased in the 2D-administered group, and in the 3D group, the $3D^{WNT}$ group had better effects than the $3D^{PLGA}$ group (Fig. 4K, L). These increases were significantly higher in the $3D^{WNT}$ group than in the 2D, $3D^{PLGA}$, suggesting that retroductal administration of EVs protection the survival of acinar, ductal structure and mucin components for up to 12 weeks post-IR.

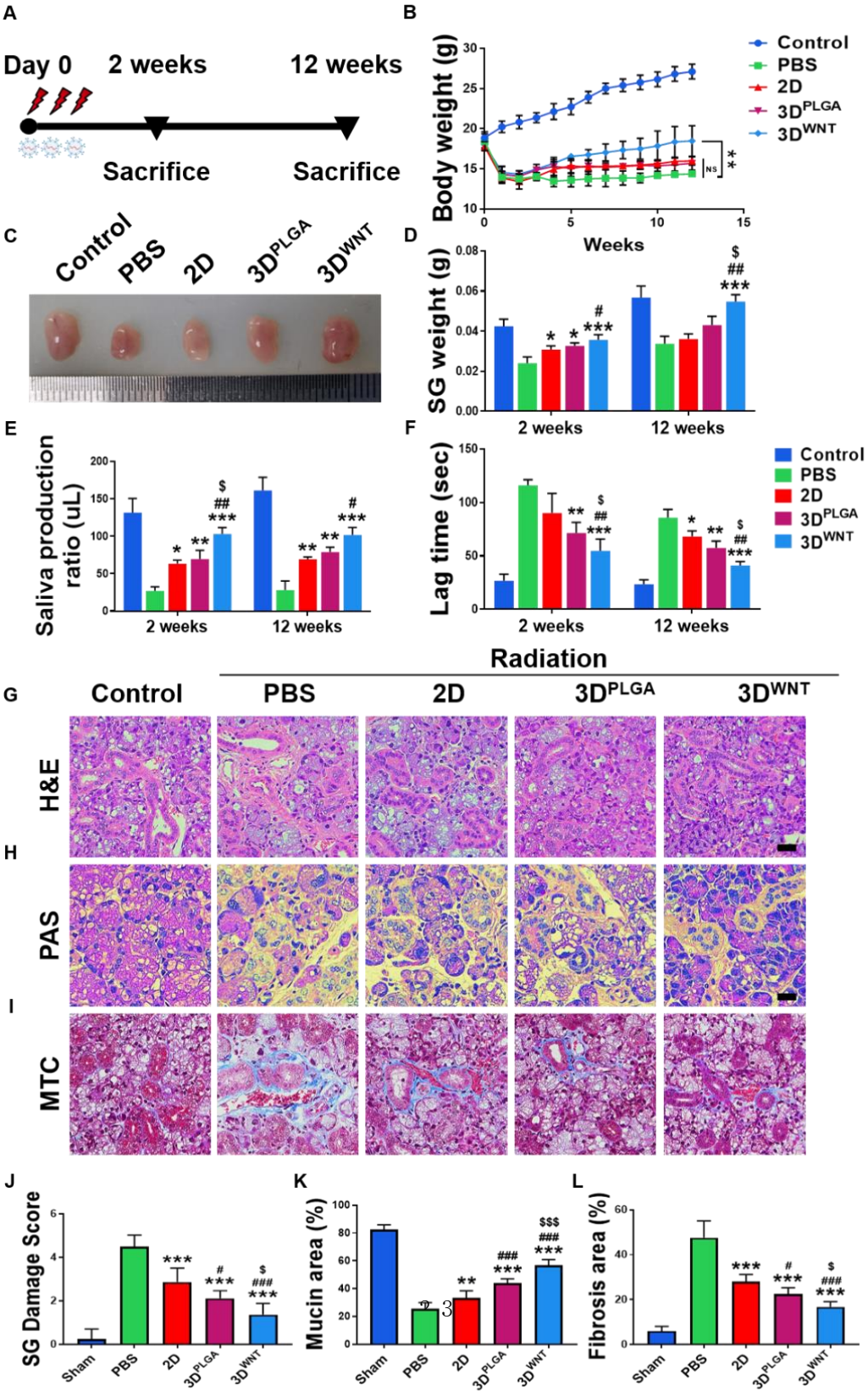

Figure 4. Retrograde exosome administration reduces radiation-related damage and preserves salivary glandular function. (A) Schematic protocol for investigating EVs in a mouse model of salivary gland hypofunction. (B) Body weight changes over time after IR. (C) Representative image of SMGs extirpated at 12 weeks after IR. (D) Salivary gland weight was measured at 12 weeks after IR. (E) Salivary total volume (μL/5 min) after stimulation at 12 weeks after IR. (F) Lag time to salivation (sec) after pilocarpine stimulation at 12 weeks after IR. Representative histological images of H&E, PAS, and MTC staining at 12 weeks post-IR (scale bar = 25 μm). Representative histological images of H&E staining at 12 weeks post-irradiation (scale bar = 25 μm). (G) Arrows indicate vacuolization. "A" and "D" indicate acinar cells and ductal cells, respectively. (H) PAS and, (I) MTC staining at 12 weeks post-irradiation (scale bar = 25 μm). Arrows indicate fibrosis. (J) Densitometric analyses were performed by measuring the pixels of the acinar and ductal areas after H&E staining; SMG damage score was quantified based on the morphological breakdown of acinar and ductal structures after H&E imaging, (K) Magenta-colored mucin production areas after PAS staining, (L) Blue fibrotic lesion areas after MTC staining. Three random fields of sections were calculated by ImageJ software. Data are presented as the mean cell number ± SEM. One-way ANOVA and Tukey's post-hoc test were used to compare groups. *compared to PBS; $^{\#}$compared to 2D; $^{\$}$compared to $3D^{PLGA}$. **P < 0.01, ***P < 0.001, $^{\#}$P < 0.05, $^{\#\#\#}$P < 0.001, $^{\$}$P < 0.05, $^{\$\$\$}$P < 0.001.

3.5. Exosomes can promote cell proliferation and exhibit an enhanced protective effect against irradiation-induced cell death and structural damage to salivary glands.

Next, we investigated the mechanism through which exosomes protect the structure and function of SMGs from radiation exposure. To examine whether exosome treatment inhibits cell death and preserves the structure and function of SMGs, we investigated whether DNA double-strand breaks (DNA-DSBs) induced by radiation contribute to cell death. Following exosome administration, we examined whether DNA-DSBs decreased. The results showed that the levels of the DNA damage marker γH2AX significantly decreased in the $3D^{WNT}$ group compared to the PBS, 2D, and $3D^{PLGA}$ groups, indicating a protective effect of exosomes on DNA damage induced by radiation (Fig. 5A). The SMG tissues in the PBS group exhibited significant DNA damage, while γH2AX-positive cells were markedly reduced in both acinar and ductal compartments in mice treated with EVs (Figure B-C). And the co-expression of caspase-3, an apoptosis marker, and $AQP5^{+}$ pro-acinar cells was observed, with a significant decrease in the number of caspase-3-expressing cells in the 2D, $3D^{PLGA}$, and $3D^{WNT}$ groups (Figure D and E). After the investigation, the number of TUNEL-positive cells significantly increased following radiation exposure. Compared to the PBS group, both the 2D, $3D^{PLGA}$, and $3D^{WNT}$ groups showed a significant decrease in the number of TUNEL-positive apoptotic cells in both acinar and ductal compartments (Figure 5(F) and (G-H)). We observed that the radioprotective effects against radiation-induced DNA damage-related cell death were significantly greater in the $3D^{WNT}$ group compared to the 2D and $3D^{PLGA}$ groups. Additionally, immunohistochemical results showed a significant increase in Ki67 expression levels in both acinar and ductal cells (Figure 5(I) and (J). These findings suggest that administering $3D^{PLGA}$ or $3D^{WNT}$ exosomes can promote cell proliferation and protect $AQP5^{+}$ pro-acinar cells from radiation-induced cellular damage. Exosomes may contribute to alleviating radiation-induced salivary gland damage and deterioration.

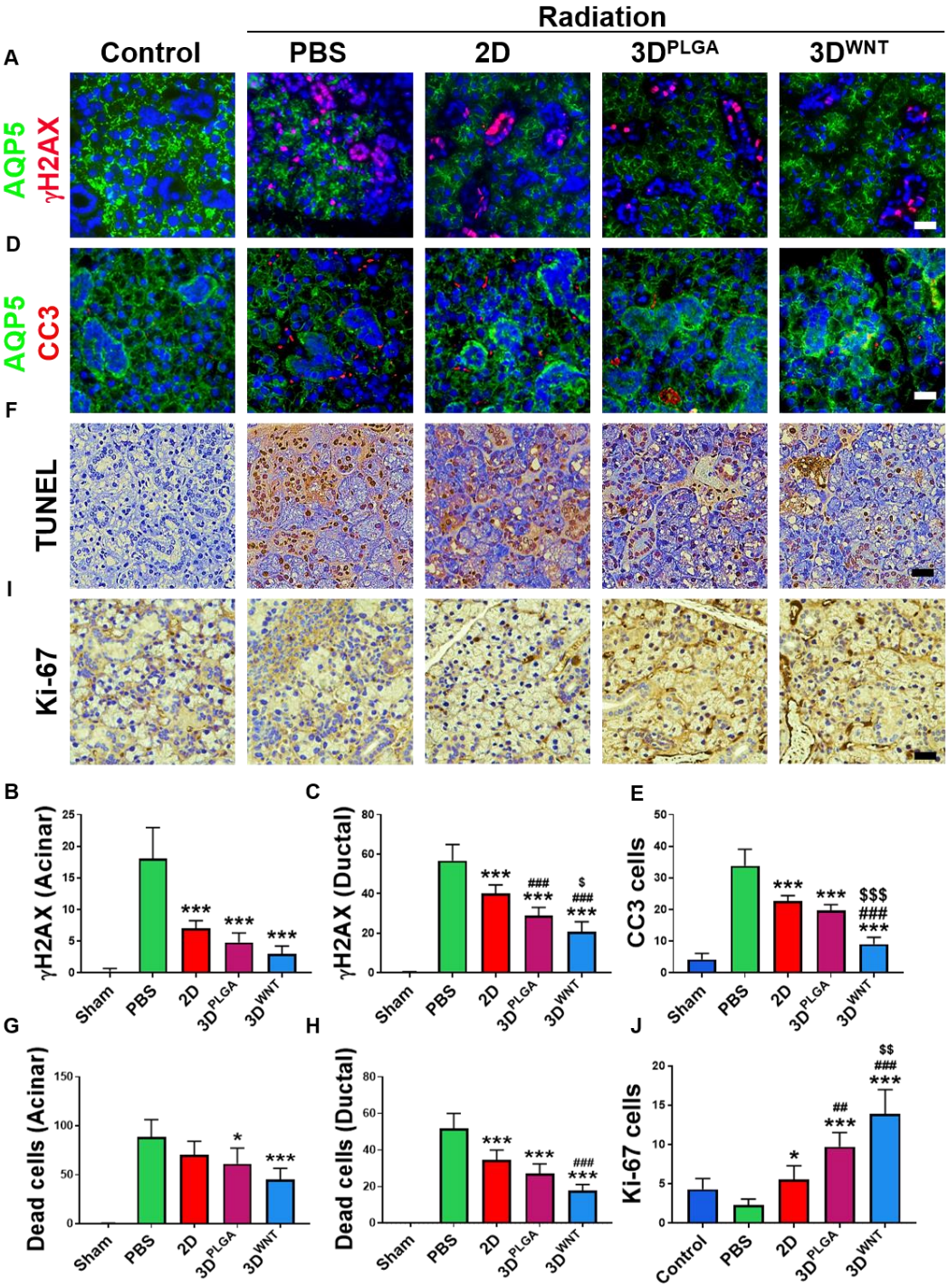

Figure 5. Exosomes extracted from 3D culture after 2 weeks post-irradiation exhibited enhanced anti-apoptotic effects and proliferative activities compared to those extracted from 2D culture. (A) Representative immunofluorescence and (B, C). quantified positive cell numbers were obtained via the γH2AX in $AQP5^+$ cells. (scale bar = 25 μm). (D) Representative immunofluorescence and (E) quantified positive cell numbers were obtained via the cleavage caspase-3 in $AQP5^+$ cells. (scale bar = 25 μm). (F) Representative immunohistochemistry and (G, H) quantified positive cell numbers were obtained via the TUNEL assay (scale bar = 25 μm). (I) Representative immunohistochemistry and (J) quantified positive cell numbers were obtained via the Ki67 assay (scale bar = 25 μm). Data are presented as the mean cell number ± SEM. One-way ANOVA and Tukey's post-hoc test were used to compare groups. *compared to PBS; $^{\#}$compared to 2D; $^{\$}$compared to $3D^{PLGA}$. *P < 0.05, **P < 0.01, ***P < 0.001, $^{\#}$P < 0.05, $^{\#\#}$P < 0.01, $^{\#\#\#}$P < 0.001, $^{\$}$P < 0.05.

3.6. Retrograde ductal infusion of exosomes promotes the survival of salivary gland progenitor cells and enhances function through the PI3K-AKT signaling pathway.

We also investigated the expression of ductal progenitor markers KRT5 and KRT7 at 2 and 12 weeks post-irradiation. Immunofluorescence staining revealed a significant increase in the expression of KRT5 and KRT7 in the $KRT5^+$ ductal progenitor cells and $KRT7^+$ luminal ductal cells in the 2D, $3D^{PLGA}$, and $3D^{WNT}$ groups compared to the PBS group (Fig. 6A and B-C). We also examined the expression of the acinar transcription factor cell, Mist1, and the pro-acinar cell marker, AQP5. Immunofluorescence staining revealed a significant increase in the expression of $Mist1^+$ acinar transcription cells and $AQP5^+$ pro-acinar cells in the 2D, $3D^{PLGA}$, and $3D^{WNT}$ groups compared to the PBS group (Fig. 6D and E). Additionally, the transcripts for Mist1 and Aqp5 decreased after irradiation but returned to control levels by 12 weeks post-IR. These results suggest that Mist1 is involved in the recovery of the salivary glands via exosomes. Therefore, despite the initial loss, AQP5 can be replenished in the acinar compartment by Mist1+ cells following radiation-induced damage. Therefore, in salivary gland tissues from mice exposed to radiation and allowed to recover for two weeks, the phosphorylation of PI3K and AKT was confirmed through immunohistochemistry (Fig. 6F, G). Compared to the group irrigated with PBS immediately after radiation exposure, overall phosphorylation of PI3K and AKT was observed to be higher in the group treated with exosomes, particularly in the $3D^{WNT}$ group (Fig. 6H, I).

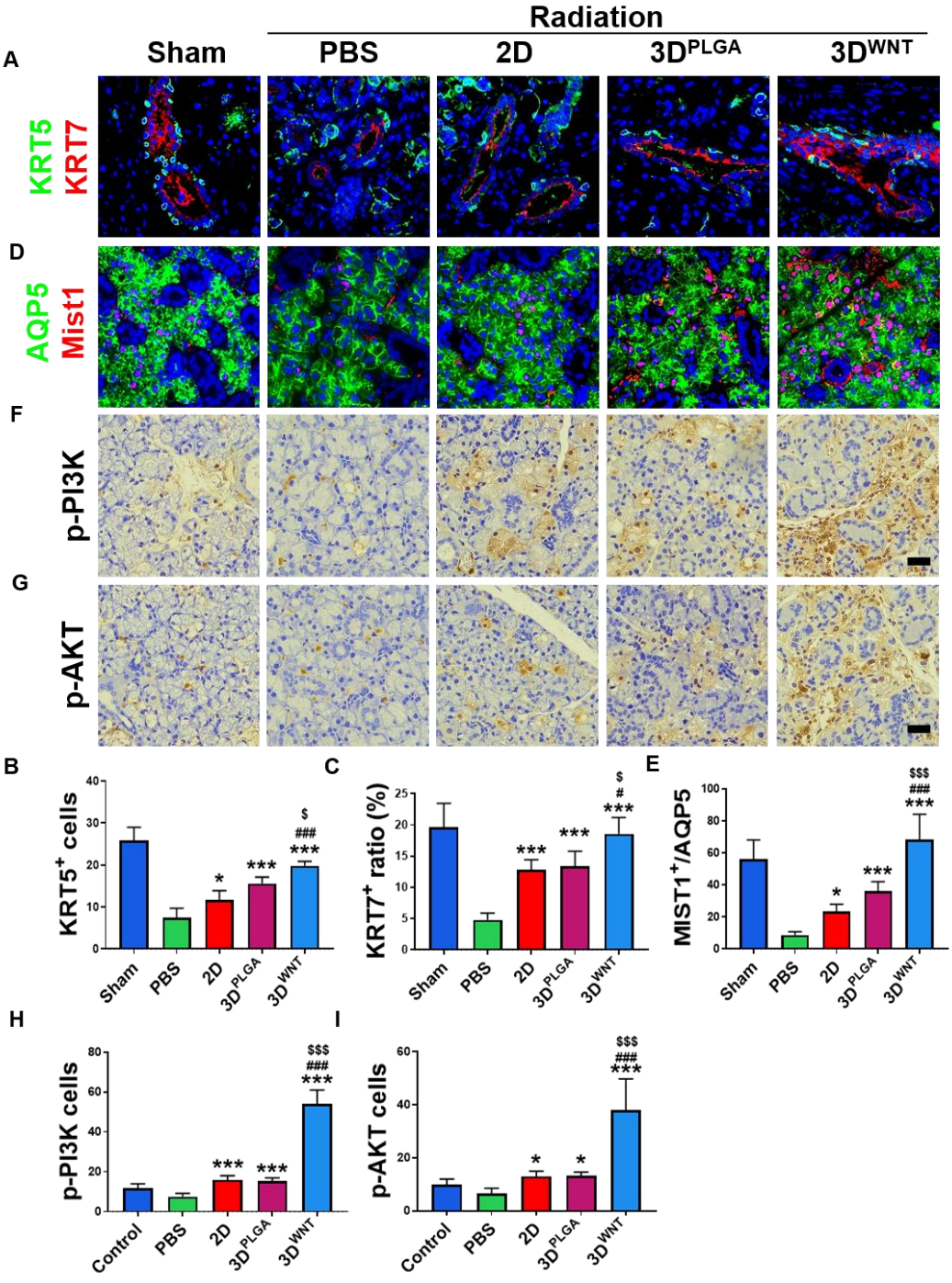

Figure 6. Retrograde exosome administration restores IR-induced salivary gland architecture and replenishes KTR5^{+}/TRT7^{+} ductal progenitors and AQP5^{+}/Mist1^{+} acinar cells. (A) Representative immunofluorescence images and (B, C) quantified positive KRT5^{+} cell number and KRT7^{+} cells. The nuclei were counterstained with DAPI (scale bar = 25 μm). (D) Representative immunofluorescence images and (E) quantified positive Mist1 + cell number in AQP5 + cells. The nuclei were counterstained with DAPI (scale bar = 25 μm). (F, G) Representative images of regulation of cell survival, growth, metabolism, and proliferation (p-PI3K, p-AKT). The scale bar indicates 25 μm. (H, I) Densitometric analyses were performed by measuring the cells of the acinar and ductal areas after p-PI3K, p-AKT; SMG survival, growth, metabolism, and proliferation score was quantified based on the morphological breakdown of acinar and ductal structures after p-PI3K, p-AKT imaging. The nuclei were counterstained with hematoxylin (scale bar = 25 μm). Data are presented as the mean cell number ± SEM. One-way ANOVA and Tukey's post-hoc test were used to compare groups. *compared to PBS; $^{\#}$compared to 2D; $^{\$}$compared to 3D^{PLGA}. *P < 0.05, **P < 0.01, ***P < 0.001, $^{\#}$P < 0.05, $^{\#\#}$P < 0.01, $^{\#\#\#}$P < 0.001, $^{\$}$P < 0.05.

3.7. Exosomes harvested from the WNT3A scaffold suppressed apoptosis and promoted growth in irradiated mouse salivary organoids.

To investigate the biological effect and differences of exosomes derived from 2D, $3D^{PLGA}$, and $3D^{WNT}$, we utilized an organoid system derived from submandibular glands (SGOs) (Fig. 7A). Firstly, we explored the optimal treatment concentration of exosomes. When exosomes from all three groups were applied to irradiated organoids, an increase in exosome concentration corresponded to an augmentation in cell viability (Fig. 7B). Therefore, we determined to use a concentration of 1x10^9 particles/mL EVs in subsequent ex vivo experiments. Radiation exposure reduced the size of SGOs and inhibited cell growth, as well as decreased the occurrence of budding or branching (Fig. 7C and F). However, exosomes derived from 2D, $3D^{PLGA}$, and $3D^{WNT}$ restored both the size of diminished SGOs and cell growth, and partially improved budding or branching in response to radiation-induced changes (Fig. 7C and F). Furthermore, exosomes derived from $3D^{WNT}$ showed superior effects compared to those derived from 2D and $3D^{PLGA}$ in increasing cell proliferation rates as assessed by radiation exposure (Fig. 7C, F, and G). Exosomes not only improved the morphology and cell growth of irradiated organoids but also enhanced mucin production, as confirmed through PAS staining (Fig. 7D, G, and H).

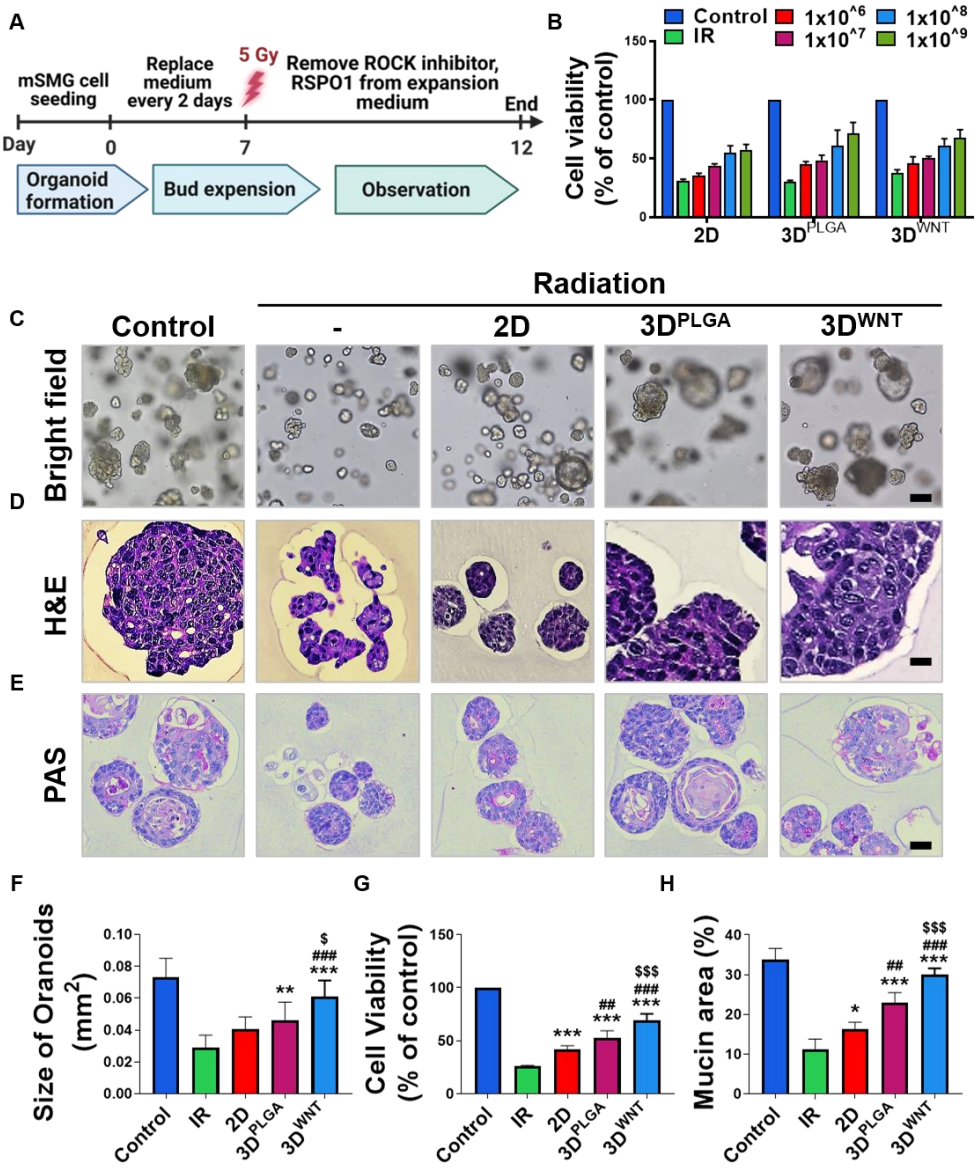

Figure 7. Exosomes mitigate radiation toxicity in salivary glands organoids derived from mice tissue. A scheme of the methodology. Schematic representation of mouse salivary gland organoid culture from salivary gland stem cells or cells isolated from the salivary gland. Produced with BioRender.com. (A) Exosome concentration testing and assessment of cell survival rates. (B) Microscopic image (phase contrast) of organoids developed from mouse salivary gland organoids

demonstrating the loss of crypt domain exposed to irradiation (C-D). Both bright field and hematoxylin and eosin (H&E) staining demonstrated complete loss of budding crypt at 5 days post-irradiation. mSMG organoids were subjected to periodic acid-Schiff staining (E). Quantification of the size of organoids by measuring the diameters of organoids (n=15, ***p < 0.001) (F). To measure viability of MSGOs, Cell Titer-Glo 3D was used at the indicated time points post-infection. Mock-infected MSGOs were used to normalize the viability as a percentage (G). Quantification of the mucin component of organoids by measuring the diameters of organoids (H). Data are presented as the mean cell number ± SEM. One-way ANOVA and Tukey's post-hoc test were used to compare groups. *compared to IR; $^{\#}$compared to 2D; $^{\$}$compared to $3D^{PLGA}$. *P < 0.05, **P < 0.01, ***P < 0.001, ##P < 0.01, ###P < 0.001, \$$P$ < 0.05, \$\$\$$P$ < 0.001).

3.8. The retroductal delivery of YWHAZ-loaded exosomes is a major pathway for regulating the regeneration of salivary gland dysfunction following irradiation.

To ascertain whether exosomes contributed to the growth of organoids by inhibiting apoptosis or promoting cell proliferation, immunofluorescent staining was conducted for markers of apoptosis, cleaved caspase-3 (CC3) (Fig. 8A, C). Exosomes not only inhibited cell death in investigated organoids but also exhibited smaller sizes and fewer branches compared to uninvestigated organoids. the sizes of irradiated and EVs-treated organoids were larger than those of irradiated and EVs-untreated organoids and, they notably stimulated cell growth, with exosomes derived from $3D^{WNT}$ showing the most potent effects. (Fig. 8A, D). Furthermore, exosomes not only promote cell growth and inhibit radiation-induced cell death but also contribute to the functional recovery of salivary gland organoids by increasing KRT14 (ductal progenitor) and AQP5 (pro-acinar cell) (Fig. 8B). Radiation-induced apoptosis can be protected by the activation of the PI3K-AKT pathway. In our study, we treated the organoids with a PI3K inhibitor (Ly294002) to investigate whether the PI3K-AKT pathway was implicated in the effects of EV pretreatment. It is known that apoptosis by radiation can be protected by the activation of PI3K-AKT. We treated the organoids with a PI3K inhibitor (Ly294002) to determine if the PI3K/AKT pathway was involved in the effects of EV pretreatment. EVs treatment decreased the levels of several apoptotic markers, including γH2AX, p-P53, P53, and cleaved caspase-3 (Fig. 8E).

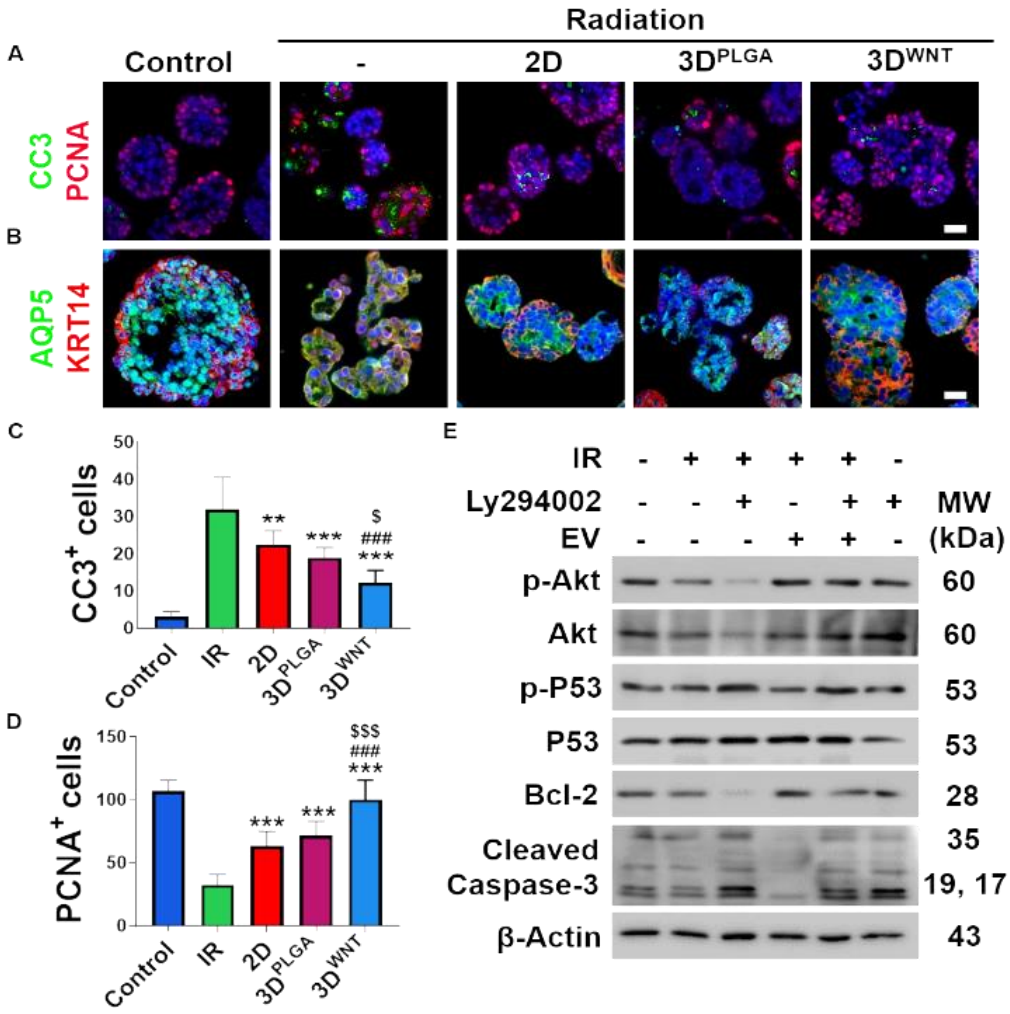

However, in the EVs pretreatment group also treated with Ly294002, IR-induced pro and anti-apoptotic markers were not alleviated. These results suggest that EV pretreatment can protect against IR through the PI3K-AKT pathway. We explored whether exosomes generated from scaffolds loaded with WNT3A exhibit superior therapeutic efficacy by analyzing the proteins encapsulated within the exosomes using LC/MS. Hierarchical clustering of $3D^{PLGA}$, and $3D^{WNT}$ EV distances by heatmap and volcano plot showed clear differences in the enriched proteins within the EV (Fig. 8E, F). When

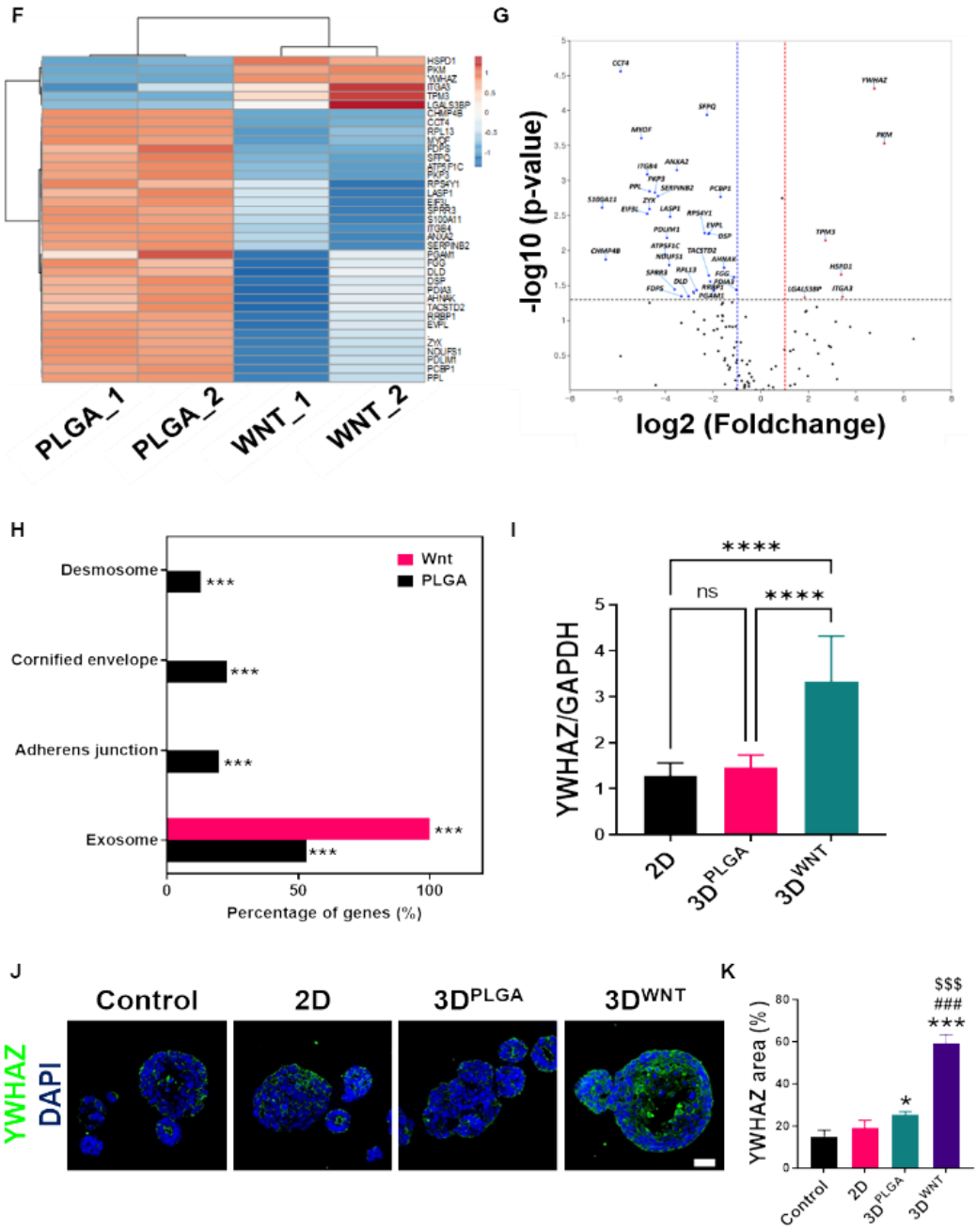

Figure 8. Proteomic analysis revealed diverse characteristics of exosomes under various conditions, including cell proliferation and anti-apoptosis of mouse salivary gland organoids.

Organoids formed in the KSFM culture medium were further cultured for an additional 5 days in the presence or absence of exosomes. (A) Representative immunofluorescence images of Caspase-3 anti-apoptosis and PCNA proliferation cells (scale bar = 25 μm) and, (B) Representative immunofluorescence images of AQP5 pro-acinar cell and KRT14 ductal progenitor cells (scale bar = 25 μm). (C,D) Quantified positive cell numbers were obtained via the CC3, PCNA positive cells (scale bar = 25 μm). (E) Western blot analysis of pro-apoptotic and anti-apoptotic protein levels after treatment of EVs with PI3K-AKT inhibitor (Ly294002). The expression levels of Cleaved caspase-3, BCL-2, p-P53, P53, p-AKT, and AKT were detected by Western blots. (F) Heat map of the protein level of shared proteins among three sources of SG-EpSC-EVs. (G) Scatter plot of log fold change versus log P value in perfusion differential expression analysis. (H) The percentage of gene products detected in proteomics experiments as a function of gene conservation. (I) Changes in expression levels of YWHAZ genes (14-3-3 zeta) were analyzed using qRT-PCR at 5 days after culture. (J) Representative immunofluorescence images of YWHAZ Genes found in the human genome. (scale bar = 25 μm). (K) Quantified positive cell numbers were obtained via the YWHAZ positive cells (scale bar = 25 μm). Data are presented as the mean cell number ± SEM. One-way ANOVA and Tukey's post-hoc test were used to compare groups. *compared to IR; $^{\#}$compared to 2D; $^{\$}$compared to $3D^{PLGA}$. $*P < 0.05$, $**P < 0.01$, ***P < 0.001, ##$P < 0.01$, ###$P < 0.001$, \$$P < 0.05$, \$\$\$$P < 0.001$).

comparing the biological properties of each internally supported protein, using Gene ontology analysis (GO) $3D^{WNT}$ showed properties for cell growth factor-related fusion, migration, and localization (Fig. 8G). Furthermore, when exosomes derived from 2D, 3DPLGA, and 3DWNT were individually administered to mouse salivary gland organoids, both mRNA and protein levels of YWHAZ were found to be highest in the 3DWNT group, as determined by qPCR analysis (Fig. 8H). Indeed, when exosomes derived from 2D, $3D^{PLGA}$, and $3D^{WNT}$ were individually administered to mouse salivary gland organoids, detection of YWHAZ through immunofluorescence staining was found to be highest in the $3D^{WNT}$ group (Fig. 8I, J). These result may imply that YWHAZ enriched $3D^{WNT}$ derived exosomes how exerts superior healing effect compared to other EVs.

Taken together, In summary, we confirmed the inhibition of cell apoptosis through the PI3K-AKT-P53 axis. This has the potential to serve as a radiation mitigator or protector, allowing selective preservation of salivary gland cells for the promotion of tissue regeneration.

In experiments where exosomes and radiation were administered to ex vivo organoids, the promotion of AKT phosphorylation by exosomes was associated with the inhibition of cell death.

4. DISCUSSION

Exosomes are considered promising for regenerative medicine. Their therapeutic efficacy can be enhanced by various isolation and culture methods. In our research, we cultivated SG-EpSCs on a WNT-secreting scaffold, which increased the secretion of exosomes and improved the healing of radiation-damaged murine salivary glands. Exosomes released by SG-EpSCs cultured on scaffolds loaded with WNT3A were found to be highly enriched with YWHAZ, which can inhibit cell death and promote cell growth. These exosomes showed a significant effect in the recovery of salivary glands in mice exposed to radiation and were verified to promote the activation of the AKT pathway through an ex vivo organoid system.

It is crucial to maintain a consistent cellular state when cultivating a large number of cells in the same volume or area for efficient and economical exosome production. While 2D cultivation allows for continuous culture without complex techniques, it is challenging to prevent overconfluence, and maintaining a consistent cell phenotype after overconfluence becomes difficult. On the other hand, 3D cultivation avoids overconfluence, allows for the cultivation of more cells in the same volume or area compared to 2D cultivation, and facilitates exosome production. However, challenges arise when using biological-derived extracellular matrix (ECM) such as Matrigel, including natural differentiation and issues like tumorigenicity. In contrast, the nanofibrous artificial ECM used in our research is free from tumorigenicity and offers the advantage of maintaining a consistent cellular state without differentiation through motif cues adjustment. Therefore, the use of nanofibrous artificial ECM may offer a highly efficient alternative for exosome production and research compared to conventional 2D cultivation or the use of biological-derived ECM.

Research on tissue healing using exosomes has mainly focused on exosomes derived from MSCs or similar stromal cells. However, recent regenerative medicine studies have looked into exosomes derived from amniotic epithelial cells or oral epithelial cells. When combined with 3D cultivation, epithelial cell-derived exosomes may be more effective than MSC-based approaches. Unlike various types of MSCs, which tend to acquire motility in a biological-derived 3D culture environment, epithelial cells do not acquire such mobility in 3D culture and maintain their inherent properties, making them advantageous for obtaining homogeneous exosomes compared to mesenchymal cells. Moreover, using epithelial cells may provide additional benefits in terms of cultivation and

maintenance compared to MSCs. By employing conditional reprogramming culture with the use of small molecules and feeder cells, it's possible to achieve an induced immortalized state, allowing the perpetuation of desirable cell properties after selective separation without the need to introduce foreign genes. Our previous research suggests that exosomes derived from autologous cells may be more advantageous for the applied tissue than stem cells from different tissues. Given that salivary glands experience a significant decrease in mesenchymal cells with maturation, and epithelial cells are dominant in the majority of salivary glands, utilizing exosomes derived from autologous salivary gland epithelial cells may be a favorable option, especially in adults. However, future research is needed to determine which cells secrete exosomes with superior efficacy, whether from epithelial or mesenchymal cells.

The WNT proteins are molecules that signal the self-renewal of WNT-dependent stem cells from various tissue origins. In a previous report, it was shown that activating the WNT pathway in 3D spheroids grown in microwells primes the functions of SGSCs, such as spheroid formation and differentiation. To investigate whether WNT proteins contribute to the promotion of stem cell properties, attempts have been made to increase their stability and activity in stem cell cultures without using serum. However, simply adding WNT proteins to a medium without FBS results in a rapid loss of WNT activity. Several approaches have been tried, such as using lipid-stabilized WNT3A, WNT3A-stabilizing serum glycoprotein afamin, and lipid-coated PLGA NPs. In this study, WNT3A proteins were encapsulated into PLGA nanofibers, allowing the release of up to 90% of the protein into the microwells over a 7-day period. The quantity of WNT3A released was sufficient to maintain stemness, and the sustained release of WNT3A significantly enhanced the paracrine and production of exosomes compared to the simple addition of recombinant WNT3A into the medium. The released paracrine factors include HGF, VEGF, IGF, BDNF, and GDNF, which are involved in salivary tissue development, remodeling, or homeostasis modulation. These findings suggest that the therapeutic potential of exosomes enriched with YWHAZ, isolated from SG-EpSCs cultured on WNT-secreting scaffolds, can enhance the improvement or regeneration of radiation-damaged salivary glands.

Recent advancements in organoid technology have led to the replacement or planned replacement of many experiments that previously relied on animal models. When studying the efficacy and mechanisms of drugs, they offer advantages over animal models in observing biological processes that occur quickly, such as protein phosphorylation and movement within the cell. However, some

disease modeling still necessitates the use of animal experiments. In particular, the chronic loss of acinar cells in salivary glands and pathological structural changes such as fibrosis caused by strong radiation exposure are challenging to observe with organoids, which undergo partial cell renewal through short-term culture or passaging. In our study, we used salivary gland organoids and found that those treated with exosomes after irradiation were larger and more numerous compared to those that were not treated. We also observed the presence of structures like lumens or endbuds. Additionally, we verified changes in protein phosphorylation and expression of specific genes under different experimental conditions using Western blotting.

In our experiments, treatment with exosomes resulted in a reduction of radiation-induced fibrosis in the salivary glands. This was especially prominent in the group with high concentrations of YWHAZ. However, further research is needed to determine whether YWHAZ directly contributes to the mitigation of fibrosis or indirectly aids in reducing fibrosis through the suppression of cell death and the subsequent inhibition of inflammation within the tissue. YWHAZ has been shown to regulate multiple intracellular biological pathways, promoting the downstream PI3K/AKT signaling. The 14-3-3z protein family participates in various signaling pathways by binding to motifs containing specific phosphoserine/phosphothreonine (pSer/Thr) residues on target proteins. YWHAZ expression is modulated by miRNAs or long non-coding RNAs, activating downstream molecules including protein kinases, apoptosis, and proliferation proteins, as well as metastasis-related molecules, thereby enhancing the potential of cell cycle progression. However, a comprehensive evaluation of YWHAZ regulatory networks through bioinformatics analysis is needed. Currently, the most widely known evidence suggests its potential role in cancer diagnosis, prognosis, and chemoresistance. However, the specificity and sensitivity of YWHAZ as an independent biomarker are limited. Combining YWHAZ with downstream targets may enhance its capability as a biomarker. Previous studies have shown that YWHAZ can form a complex with β-catenin to activate the WNT signaling pathway, enhancing cell growth potential. This result aligns with our study, indicating that YWHAZ may increase radiation-induced apoptosis and proliferation both in vitro and in vivo, possibly through the PI3K/AKT axis.

Salivary gland cancers, particularly those in the head and neck region, are currently treated with standard therapies involving surgery and CCRT. However, salivary glands are highly sensitive to radiation, and radiation damage can cause permanent impairment of salivary gland function. While attempts have been made to use gene therapy and growth factors to prevent or reverse salivary gland

dysfunction, these approaches have not yet been widely adopted in clinical practice. Specifically, the use of growth factors is limited due to the potential to stimulate the survival and growth of remaining cancer cells. Proteomic analysis has shown an enrichment of YWHAZ in salivary gland epithelial cells enhanced with WNT. Interestingly, YWHAZ is known to be overexpressed in many types of malignant tumors, promoting resistance to anticancer treatments and tumor growth. However, it has been reported that its expression is suppressed in salivary gland tumors. This presents an opportunity for the safe use of exosomes derived from WNT-enhanced salivary gland epithelial cells to address radiation-induced salivary gland dysfunction. Further research is needed to understand how YWHAZ can be efficiently encapsulated within exosomes during WNT enhancement.

5. CONCLUSION

Our research findings show that exosomes from WNT-enhanced SG-EpSCs can help repair radiation-damaged mouse salivary glands. They achieve this by delivering YWHAZ, which helps resist cell apoptosis and promotes cell growth. This study proposes a new therapeutic approach and molecular mechanism for restoring impaired salivary gland function using exosomes. The proposed approach involves providing autologous salivary gland epithelial cells before radiotherapy in salivary and head and neck cancer patients.

REGERENCES

1. Alevizos I, Zheng C, Cotrim AP, Liu S, McCullagh L, Billings ME, Goldsmith CM, Tandon M, Helmerhorst EJ, Catalán MA, et al. 2017. Late responses to adenoviral-mediated transfer of the aquaporin-1 gene for radiation-induced salivary hypofunction. Gene Ther. 24(3):176–186.
2. Arany S, Benoit DS, Dewhurst S, Ovitt CE. 2013. Nanoparticle-mediated gene silencing confers radioprotection to salivary glands in vivo. Mol Ther. 21(6):1182–1194.
3. Aure MH, Arany S, Ovitt CE. 2015. Salivary glands: stem cells, self-duplication, or both? J Dent Res. 94(11):1502–1507.
4. Baum BJ, Alevizos I, Zheng C, Cotrim AP, Liu S, McCullagh L, Goldsmith CM, Burbelo PD, Citrin DE, Mitchell JB, et al. 2012. Early responses to adenoviral-mediated transfer of the aquaporin-1 cDNA for radiationinduced salivary hypofunction. Proc Natl Acad Sci USA. 109(47):1940319407.
5. Baum BJ, Zheng C, Alevizos I, Cotrim AP, Liu S, McCullagh L, Goldsmith CM, McDermott N, Chiorini JA, Nikolov NP, et al. 2010. Development of a gene transfer-based treatment for radiation-induced salivary hypofunction. Oral Oncol. 46(1):4–8.
6. Björkelund H, Gedda L, Andersson K. 2011. Comparing the epidermal growth factor interaction with four different cell lines: intriguing effects imply strong dependency of cellular context. PLoS One. 6(1):e16536.
7. Cheng SC, Wu VW, Kwong DL, Ying MT. 2011. Assessment of post-radiotherapy salivary glands. Br J Radiol. 84(1001):393–402.
8. Delporte C, O'Connell BC, He X, Lancaster HE, O'Connell AC, Agre P, Baum BJ. 1997. Increased fluid secretion after adenoviral-mediated transfer of the aquaporin-1 cDNA to irradiated rat salivary glands. Proc Natl Acad Sci U S A. 94(7):3268–3273.
9. Emmerson E, Knox SM. 2018. Salivary gland stem cells: a review of development, regeneration and cancer. Genesis. 56(5):e23211.
10. Ferreira JNA, Zheng C, Lombaert IMA, Goldsmith CM, Cotrim AP, Symonds JM, Patel VN, Hoffman MP. 2018. Neurturin gene therapy protects parasympathetic function to prevent irradiation-induced murine salivary gland hypofunction. Mol Ther Methods Clin Dev. 9:172–180.
11. Grundmann O, Mitchell GC, Limesand KH. 2009. Sensitivity of salivary glands to radiation: from animal models to therapies. J Dent Res. 88(10):894–903.
12. Kim JW, Kim JM, Choi ME, Kim SK, Kim YM, Choi JS. 2019. Adiposederived mesenchymal stem cells regenerate radioiodine-induced

salivary gland damage in a murine model. Sci Rep. 9(1):15752.

13. Krall JA, Beyer EM, MacBeath G. 2011. High- and low-affinity epidermal growth factor receptor-ligand interactions activate distinct signaling pathways. PLoS One. 6(1):e15945.
14. Kuriki Y, Liu Y, Xia D, Gjerde EM, Khalili S, Mui B, Zheng C, Tran SD. 2011. Cannulation of the mouse submandibular salivary gland via the Wharton's duct. J Vis Exp. (51):3074.
15. Kwak M, Alston N, Ghazizadeh S. 2016. Identification of stem cells in the secretory complex of salivary glands. *J Dent Res*. 95(7):776–783.
16. Lim JY, Ra JC, Shin IS, Jang YH, An HY, Choi JS, Kim WC, Kim YM. 2013. Systemic transplantation of human adipose tissue-derived mesenchymal stem cells for the regeneration of irradiation-induced salivary gland damage. *PLoS One*. 8(8):e71167.
17. Lim JY, Yi T, Choi JS, Jang YH, Lee S, Kim HJ, Song SU, Kim YM. 2013. Intraglandular transplantation of bone marrow-derived clonal mesenchymal stem cells for amelioration of post-irradiation salivary gland damage. *Oral Oncol*. 49(2):136–143.
18. Limesand KH, Avila JL, Victory K, Chang HH, Shin YJ, Grundmann O, Klein RR. 2010. Insulin-like growth factor-1 preserves salivary gland function after fractionated radiation. *Int J Radiat Oncol Biol Phys*. 78(2):579–586.
19. Lombaert I, Movahednia MM, Adine C, Ferreira JN. 2017. Concise review: salivary gland regeneration: therapeutic approaches from stem cells to tissue organoids. *Stem Cells*. 35(1):97–105.
20. Lombaert IM, Knox SM, Hoffman MP. 2011. Salivary gland progenitor cell biology provides a rationale for therapeutic salivary gland regeneration. *Oral Dis*. 17(5):445–449.
21. Maimets M, Rocchi C, Bron R, Pringle S, Kuipers J, Giepmans BN, Vries RG, Clevers H, de Haan G, van Os R, et al. 2016. Long-term in vitro expansion of salivary gland stem cells driven by Wnt signals. *Stem Cell Reports*. 6(1):150–162.
22. Marmary Y, Adar R, Gaska S, Wygoda A, Maly A, Cohen J, Eliashar R, Mizrachi L, Orfaig-Geva C, Baum BJ, et al. 2016. Radiation-induced loss of salivary gland function is driven by cellular senescence and prevented by IL6 modulation. *Cancer Res*. 76(5):1170–1180.
23. May AJ, Cruz-Pacheco N, Emmerson E, Gaylord EA, Seidel K, Nathan S, Muench MO, Klein OD, Knox SM. 2018. Diverse progenitor cells preserve salivary gland ductal architecture after radiation-induced damage. *Development*. 145(21):dev166363.
24. Nair RP, Zheng C, Sunavala-Dossabhoy G. 2016. Retroductal

submandibular gland instillation and localized fractionated irradiation in a rat model of salivary hypofunction. *J Vis Exp*. (110):53785.

25. Najafi S, Nosrati H, Faraji Z, Mohamadnia A, Shirian S, Mortazavi SM, Bahrami N. 2020. Reconstruction of necrotic submandibular salivary gland using mesenchymal stem cells. *Heliyon*. 6(10):e05162.
26. Nam K, Maruyama CL, Trump BG, Buchmann L, Hunt JP, Monroe MM, Baker OJ. 2016. Post-irradiated human submandibular glands display high collagen deposition, disorganized cell junctions, and an increased number of adipocytes. *J Histochem Cytochem*. 64(6):343–352.
27. Qiu W, Leibowitz B, Zhang L, Yu J. 2010. Growth factors protect intestinal stem cells from radiation-induced apoptosis by suppressing PUMA through the PI3K/AKT/p53 axis. *Oncogene*. 29(11):1622–1632.
28. Redman RS, Ball WD, Mezey E, Key S. 2009. Dispersed donor salivary gland cells are widely distributed in the recipient gland when infused up the ductal tree. *Biotech Histochem*. 84(6):253–260.
29. Shin HS, An HY, Choi JS, Kim HJ, Lim JY. 2017. Organotypic spheroid culture to mimic radiation-induced salivary hypofunction. *J Dent Res*. 96(4):396–405.
30. Shin HS, Lee S, Kim YM, Lim JY. 2018. Hypoxia-activated adipose mesenchymal stem cells prevents irradiation-induced salivary hypofunction by enhanced paracrine effect through fibroblast growth factor 10. *Stem Cells*. 36(7):1020–1032.
31. Sunavala-Dossabhoy G, Palaniyandi S, Richardson C, De Benedetti A, Schrott L, Caldito G. 2012. TAT-mediated delivery of Tousled protein to salivary glands protects against radiation-induced hypofunction. *Int J Radiat Oncol Biol Phys*. 84(1):257–265.
32. Varghese JJ, Schmale IL, Mickelsen D, Hansen ME, Newlands SD, Benoit DSW, Korshunov VA, Ovitt CE. 2018. Localized delivery of amifostine enhances salivary gland radioprotection. *J Dent Res*. 97(11):1252–1259.
33. Varghese JJ, Schmale IL, Wang Y, Hansen ME, Newlands SD, Ovitt CE, Benoit DSW. 2018. Retroductal nanoparticle injection to the murine submandibular gland. *J Vis Exp*. (135):57521.
34. Weng PL, Aure MH, Maruyama T, Ovitt CE. 2018. Limited regeneration of adult salivary glands after severe injury involves cellular plasticity. *Cell Rep*. 24(6):1464–1470.e3.
35. Xu R, Sun Y, Chen Z, Yao Y, Ma G. 2016. Hypoxic preconditioning inhibits hypoxia-induced apoptosis of cardiac progenitor cells via the PI3K/Akt-DNMT1-p53 pathway. *Sci Rep*. 6:30922.
36. Yoon YJ, Shin HS, Lim JY. 2019. A hepatocyte growth factor/MET-induced

antiapoptotic pathway protects against radiation-induced salivary gland dysfunction. *Radiother Oncol*. 138:9–16.

37. Zheng C, Cotrim AP, Rowzee A, Swaim W, Sowers A, Mitchell JB, Baum BJ. 2011. Prevention of radiation-induced salivary hypofunction following hKGF gene delivery to murine submandibular glands. *Clin Cancer Res*. 17(9):2842–2851.
38. Zheng C, Goldsmith CM, Mineshiba F, Chiorini JA, Kerr A, Wenk ML, Vallant M, Irwin RD, Baum BJ. 2006. Toxicity and biodistribution of a first-generation recombinant adenoviral vector, encoding aquaporin-1, after retroductal delivery to a single rat submandibular gland. *Hum Gene Ther*. 17(11):1122–1133.
39. Jensen DH, Oliveri RS, Trojahn Kølle SF, et al. Mesenchymal stem cell therapy for salivary gland dysfunction and xerostomia: a systematic review of preclinical studies. *Oral Surg Oral Med Oral Pathol Oral Radiol* 2014; 117: 335–342.e1.
40. Karp JM, Leng Teo GS. Mesenchymal stem cell homing: the devil is in the details. *Cell Stem Cell* 2009; 4: 206–216.
41. Foster AA, Marquardt LM, Heilshorn SC. The diverse roles of hydrogel mechanics in injectable stem cell transplantation. *Curr Opin Chem Eng* 2017; 15: 15–23.
42. Kim SJ, Kim EM, Yamamoto M, et al. Engineering multi-cellular spheroids for tissue engineering and regenerative medicine. *Adv Healthc Mater* 2020; 2020: e2000608.
43. Xu Y, Shi T, Xu A, et al. 3D spheroid culture enhances survival and therapeutic capacities of MSCs injected into ischemic kidney. *J Cell Mol Med* 2016; 20: 1203–1213.
44. Cho RJ, Kim YS, Kim JY, et al. Human adipose-derived mesenchymal stem cell spheroids improve recovery in a mouse model of elastase-induced emphysema. *BMB Rep* 2017; 50: 79–84.
45. Kim M, Yun HW, Park DY, et al. Three-dimensional spheroid culture increases exosome secretion from mesenchymal stem cells. *Tissue Eng Regen Med* 2018; 15: 427–436.
46. Kim JH, Lee JY. Multi-spheroid-loaded human acellular dermal matrix carrier preserves its spheroid shape and improves in vivo adipose-derived stem cell delivery and engraftment. *Tissue Eng Regen Med* 2020; 17: 565–566.
47. Lv D, Hu Z, Lu L, et al. Three-dimensional cell culture: A powerful tool in tumor research and drug discovery. *Oncol Lett* 2017; 14: 6999–7010.
48. Lin RZ, Chang HY. Recent advances in three-dimensional multicellular

spheroid culture for biomedical research. *Biotechnol J* 2008; 3: 1172–1184.
49. Sakai Y, Nakazawa K. Technique for the control of spheroid diameter using microfabricated chips. *Acta Biomater* 2007; 3: 1033–1040.
50. Li Z, Guo X, Sun L, et al. A simple microsphere-based mold to rapidly fabricate microwell arrays for multisize 3D tumor culture. *Biotechnol Bioeng* 2020; 117: 1092–1100.
51. Liu D, Chen S, Win Naing M. A review of manufacturing capabilities of cell spheroid generation technologies and future development. *Biotechnol Bioeng* 2021; 118: 542–554.
52. Agarwal S, Wendorff JH, Greiner A. Use of electrospinning technique for biomedical applications. *Polymer* 2008; 49: 5603–5621.
53. Lee HJ, Koh WG. Hydrogel micropattern-incorporated fibrous scaffolds capable of sequential growth factor delivery for enhanced osteogenesis of hMSCs. *ACS Appl Mater Interfaces* 2014; 6: 9338–9348.
54. Lee HJ, Kim HS, Kim HO, et al. Micropatterns of double-layered nanofiber scaffolds with dual functions of cell patterning and metabolite detection. *Lab Chip* 2011; 11: 2849–2857.
55. Chua KN, Lim WS, Zhang P, et al. Stable immobilization of rat hepatocyte spheroids on galactosylated nanofiber scaffold. *Biomaterials* 2005; 26: 2537–2547.
56. Lee HW, Kook Y-M, Lee HJ, et al. A three-dimensional co-culture of HepG2 spheroids and fibroblasts using double-layered fibrous scaffolds incorporated with hydrogel micropatterns. *RSC Adv* 2014; 4: 61005–61011.
57. Shin HS, Lee S, Hong HJ, et al. Stem cell properties of human clonal salivary gland stem cells are enhanced by three-dimensional priming culture in nanofibrous microwells. *Stem Cell Res Ther* 2018; 9: 74.
58. Cooperstein MA, Canavan HE. Biological cell detachment from poly(N-isopropyl acrylamide) and its applications. *Langmuir* 2010; 26: 7695–7707.
59. Nakajima K, Honda S, Nakamura Y, et al. Intact microglia are cultured and non-invasively harvested without pathological activation using a novel cultured cell recovery method. *Biomaterials* 2001; 22: 1213–1223.
60. Tang Z, Okano T. Recent development of temperature-responsive surfaces and their application for cell sheet engineering. *Regen Biomater* 2014; 1(1): 91–102.
61. Yang J, Yamato M, Kohno C, et al. Cell sheet engineering: recreating tissues without biodegradable scaffolds. *Biomaterials* 2005; 26: 6415–6422.
62. Baum BJ, Alevizos I, Zheng C, Cotrim AP, Liu S, McCullagh L, Goldsmith CM, Burbelo PD, Citrin DE, Mitchell JB, et al. 2012. Early responses to adenoviral-mediated transfer of the aquaporin-1 cDNA for radiationinduced

salivary hypofunction. Proc Natl Acad Sci USA. 109(47):1940319407.
63. Baum BJ, Alevizos I, Zheng C, Cotrim AP, Liu S, McCullagh L, Goldsmith CM, Burbelo PD, Citrin DE, Mitchell JB, et al. 2012. Early responses to adenoviral-mediated transfer of the aquaporin-1 cDNA for radiationinduced salivary hypofunction. Proc Natl Acad Sci USA. 109(47):1940319407.
64. Baum BJ, Alevizos I, Zheng C, Cotrim AP, Liu S, McCullagh L, Goldsmith CM, Burbelo PD, Citrin DE, Mitchell JB, et al. 2012. Early responses to adenoviral-mediated transfer of the aquaporin-1 cDNA for radiationinduced salivary hypofunction. Proc Natl Acad Sci USA. 109(47):1940319407.
65. Baum BJ, Alevizos I, Zheng C, Cotrim AP, Liu S, McCullagh L, Goldsmith CM, Burbelo PD, Citrin DE, Mitchell JB, et al. 2012. Early responses to adenoviral-mediated transfer of the aquaporin-1 cDNA for radiationinduced salivary hypofunction. Proc Natl Acad Sci USA. 109(47):1940319407.
66. Chen M, Dong M, Havelund R, et al. Thermo-responsive Core−Sheath electrospun nanofibers from poly (N-isopropylacrylamide)/polycaprolactone blends. *Chem Mater* 2010; 22: 4214–4221.
67. Yi T, Lee S, Choi N, et al. Single cell clones purified from human parotid glands display features of multipotent epitheliomesenchymal stem cells. *Sci Rep* 2016; 6: 36303.
68. Cho JM, Yun SM, Choi YH, et al. Xanthohumol prevents dextran sulfate sodium-induced colitis via inhibition of IKKβ/NF-κB signaling in mice. *Oncotarget* 2018; 9: 866–880.
69. Rockwood DN, Chase DB, Akins RE, et al. Characterization of electrospun poly(N-isopropyl acrylamide) fibers. *Polymer* 2008; 49: 4025–4032.
70. Gu SY, Wang Z-M, Li JB, et al. Switchable wettability of thermo-responsive biocompatible nanofibrous films created by electrospinning. *Macromol Mater Eng* 2010; 295: 32–36.
71. Foraida ZI, Kamaldinov T, Nelson DA, et al. Elastin-PLGA hybrid electrospun nanofiber scaffolds for salivary epithelial cell self-organization and polarization. *Acta Biomater* 2017; 62: 116–127.
72. Chan YH, Huang TW, Chou YS, et al. Formation of post-confluence structure in human parotid gland acinar cells on PLGA through regulation of E-cadherin. *Biomaterials* 2012; 33: 464–472.
73. Chou YS, Young TH, Lou PJ. Effects of biomaterial-derived fibroblast conditioned medium on the α-amylase expression of parotid gland acinar cells. *Acta Biomater* 2015; 27: 214–223.
74. Shubin AD, Felong TJ, Schutrum BE, et al. Encapsulation of primary salivary gland cells in enzymatically degradable poly(ethylene glycol)

hydrogels promotes acinar cell characteristics. *Acta Biomater* 2017; 50: 437–449.

75. Lee HW, Hsiao YC, Young TH, et al. Maintenance of the spheroid organization and properties of glandular progenitor cells by fabricated chitosan based biomaterials. *Biomater Sci* 2018; 6: 1445–1456.
76. Nam K, Jones JP, Lei P, et al. Laminin-111 peptides conjugated to fibrin hydrogels promote formation of lumen containing parotid gland cell clusters. *Biomacromolecules* 2016; 17: 2293–2301.
77. Nam K, Wang CS, Maruyama CLM, et al. L1 peptide-conjugated fibrin hydrogels promote salivary gland regeneration. *J Dent Res* 2017; 96: 798–806.
78. Ozdemir T, Fowler EW, Liu S, et al. Tuning hydrogel properties to promote the assembly of salivary gland spheroids in 3D. *ACS Biomater Sci Eng* 2016; 2: 2217–2230.
79. Srinivasan PP, Patel VN, Liu S, et al. Primary salivary human stem/progenitor cells undergo microenvironment-driven acinar-like differentiation in hyaluronate hydrogel culture. *Stem Cells Transl Med* 2017; 6: 110–120.
80. Maria OM, Liu Y, El-Hakim M, et al. The role of human fibronectin- or placenta basement membrane extract-based gels in favouring the formation of polarized salivary acinar-like structures. *J Tissue Eng Regen Med* 2017; 11: 2643–2657.
81. Bécavin T, Kuchler-Bopp S, Kökten T, et al. Well-organized spheroids as a new platform to examine cell interaction and behaviour during organ development. *Cell Tissue Res* 2016; 366: 601–615.
82. Soscia DA, Sequeira SJ, Schramm RA, et al. Salivary gland cell differentiation and organization on micropatterned PLGA nanofiber craters. *Biomaterials* 2013; 34: 6773–6784.
83. Shin HS, Kook YM, Hong HJ, et al. Functional spheroid organization of human salivary gland cells cultured on hydrogel-micropatterned nanofibrous microwells. *Acta Biomater* 2016; 45: 121–132.
84. Rothova M, Thompson H, Lickert H, et al. Lineage tracing of the endoderm during oral development. *Dev Dyn* 2012; 241: 1183–1191.
85. Kwon HR, Larsen M. The contribution of specific cell subpopulations to submandibular salivary gland branching morphogenesis. *Curr Opin Genet Dev* 2015; 32: 47–54.
86. Zhang H, Boddupally K, Kandyba E, et al. Defining the localization and molecular characteristic of minor salivary gland label-retaining cells. *Stem Cells* 2014; 32: 2267–2277.

87. Kwak M, Alston N, Ghazizadeh S. Identification of stem cells in the secretory complex of salivary glands. *J Dent Res* 2016; 95: 776–783.
88. Chibly AM, Querin L, Harris Z, et al. Label-retaining cells in the adult murine salivary glands possess characteristics of adult progenitor cells. *PLoS One* 2014; 9: e107893.
89. Bullard T, Koek L, Roztocil E, et al. Ascl3 expression marks a progenitor population of both acinar and ductal cells in mouse salivary glands. *Dev Biol* 2008; 320: 72–78.
90. Nelson DA, Manhardt C, Kamath V, et al. Quantitative single cell analysis of cell population dynamics during submandibular salivary gland development and differentiation. *Biol Open* 2013; 2: 439–447.
91. Emmerson E, May AJ, Berthoin L, et al. Salivary glands regenerate after radiation injury through SOX2-mediated secretory cell replacement. *EMBO Mol Med* 2018; 10(3): e8051.
92. Cho JM, Yoon YJ, Lee S, et al. Retroductal delivery of epidermal growth factor protects salivary progenitors after irradiation. *J Dent Res* 2021; 100: 883–890.
93. Yoon YJ, Shin HS, Lim JY. A hepatocyte growth factor/MET-induced antiapoptotic pathway protects against radiation-induced salivary gland dysfunction. *Radiother Oncol* 2019; 138: 9–16.
94. Shin HS, Lee S, Kim YM, et al. Hypoxia-activated adipose mesenchymal stem cells prevents irradiation-induced salivary hypofunction by enhanced paracrine effect through fibroblast growth factor 10. *Stem Cells* 2018; 36: 1020–1032.
95. Grundmann O, Fillinger JL, Victory KR, et al. Restoration of radiation therapy-induced salivary gland dysfunction in mice by post therapy IGF-1 administration. *BMC Cancer* 2010; 10: 417.
96. Meyer S, Chibly AM, Burd R, et al. Insulin-like growth Factor-1-Mediated DNA repair in irradiated salivary glands is sirtuin-1 dependent. *J Dent Res* 2017; 96: 225–232.
97. Zhang S, Sui Y, Fu X, et al. Specific complexes derived from extracellular matrix facilitate generation of structural and drug-responsive human salivary gland microtissues through maintenance stem cell homeostasis. *J Tissue Eng Regen Med* 2020; 14: 284–294.
98. Pringle S, Maimets M, van der Zwaag M, et al. Human salivary gland stem cells functionally restore radiation damaged salivary glands. *Stem Cells* 2016; 34: 640–652.
99. H.S. Shin, H.J. Hong, W.G. Koh, J.Y. Lim, Organotypic 3D Culture in Nanoscaffold Microwells Supports Salivary Gland Stem-Cell-Based Organization,

ACS Biomater Sci Eng. 4 (2018) 4311–4320.

100. Front. Cell Dev. Biol., 17 September 2020 Sec. Molecular and Cellular Pathology Immune (Cell) Derived Exosome Mimetics (IDEM) as a Treatment for Ovarian Cancer

101. Mendez-Barbero N, Gutierrez-Munoz C, Madrigal-Matute J, Minguez P, Egido J, Michel JB, Martin-Ventura JL, Esteban V, Blanco-Colio LM. A major role of TWEAK/Fn14 axis as a therapeutic target for post-angioplasty restenosis. EBioMedicine. 2019;46:274–89.

102. Spadaccio C, Antoniades C, Nenna A, Chung C, Will R, Chello M, Gaudino MFL. Preventing treatment failures in coronary artery disease: what can we learn from the biology of in-stent restenosis, vein graft failure, and internal thoracic arteries? Cardiovasc Res. 2020;116(3):505–19.

103. Na, K.; Shin, H.; Cho, J. Y.; Jung, S. H.; Lim, J.; Lim, J. S.; Kim, E. A.; Kim, H. S.; Kang, A. R.; Kim, J. H.; Shin, J. M.; Jeong, S. K.; Kim, C. Y.; Park, J. Y.; Chung, H. M.; Omenn, G. S.; Hancock, W. S.; Paik, Y. K. Systematic Proteogenomic Approach To Exploring a Novel Function for NHERF1 in Human Reproductive Disorder: Lessons for Exploring Missing Proteins. *J. Proteome*

104. 3D Organoid Culture From Adult Salivary Gland Tissues as an ex vivo Modeling of Salivary Gland Morphogenesis

105. J M Cho , Y J Yoon , S Lee , D Kim 1, D Choi , J Kim , J Y Lim Retroductal Delivery of Epidermal Growth Factor Protects Salivary Progenitors after Irradiation. J Dent Res. 2021 Jul;100(8):883-890.

106. Hye Jin Hong, Jae-Min Cho, Yeo-Jun Yoon, DoJin Choi, Soohyun Lee, Hwajung Lee, Sujeong Ahn, Won-Gun Koh, Jae-Yol Lim. Thermoresponsive fiber-based microwells capable of formation and retrieval of salivary gland stem cell spheroids for the regeneration of irradiation-damaged salivary glands. J Tissue Eng. 2022 Apr 7:13:20417314221085645.

Abstract in Korean

Wnt가 탑재된 마이크로웰 배양에서 생산된 타액선 줄기 세포 유래 엑소좀은 쥐 타액선 손상 모델에서 타액선 기능 장애로부터의 회복을 가속화합니다.

본 논문은 지속적인 WNT3A 방출이 있는 3차원 마이크로웰 스캐폴드에서 생산된 타액선 줄기세포 유래 엑소좀의 재생 효과를 조사하기 위한 연구를 진행했습니다. 이 연구는 방사선에 노출된 쥐의 타액선의 기능에 대한 조사를 중점적으로 다루었습니다. 새로운 배양방법이 유전자 표지자 발현, 측분비 기능, 그리고 분화 잠재력 측면에서 줄기세포를 촉진하는지 여부를 결정하고, 3차원 스페로이드 배양에서 줄기세포 촉진의 역할을 조사했습니다.

이를 위해 WNT 가 로드된 나노섬유를 사용하여 PCL 마이크로웰 스캐폴드와 결합되었고, 지속적인 WNT 방출을 가능하게 하기 위해 WNT3A 단백질이 로드된 PLGA 나노섬유가 제조되었습니다. 인간 타액선에서 유래된 상피 줄기세포는 2차원(단일세포) 또는 3차원 PLGA 나노섬유-PCL 마이크로웰 (3DPLGA) 및 WNT 로드된 PLGA 나노섬유-PCL 마이크로웰 (3DWNT)에 배양되었습니다.

우리는 배양 매체에서 초원심분리기를 이용하여 분리한 기능성 엑소좀을 역행적으로 쥐의 타액관에 주입하고, 쥐의 타액선 손상 모델에서 타액선 기능 회복에 대한 타액선 줄기세포 유래 엑소좀의 재생 잠재력을 조사했습니다. 결과적으로, 마이크로웰 스캐폴드에 배양된 줄기세포는 모두 3차원 스페로이드를 형성했으며, 3DWNT 의 스페로이드는 3DPLGA 에 비해 줄기세포 관련 유전자 및 단백질 발현이 현저하게 더 높았으며, 더 많은 양의 엑소좀을 생산하고 측분비 활동이 향상되었습니다.

핵심되는 말 : 3차원배양, 마이크로웰, WNT3A방출, 엑소좀, 타액선.